ARTICLE

Detection of Ca²⁺ transients near ryanodine receptors by targeting fluorescent Ca²⁺ sensors to the triad

Colline Sanchez[1], Christine Berthier[1] , Yves Tourneur[2] , Laloé Monteiro[1], Bruno Allard[1] , Laszlo Csernoch[3] , and Vincent Jacquemond[1]

In intact muscle fibers, functional properties of ryanodine receptor (RYR)–mediated sarcoplasmic reticulum (SR) Ca²⁺ release triggered by activation of the voltage sensor Ca$_V$1.1 have so far essentially been addressed with diffusible Ca²⁺-sensitive dyes. Here, we used a domain (T306) of the protein triadin to target the Ca²⁺-sensitive probe GCaMP6f to the junctional SR membrane, in the immediate vicinity of RYR channels, within the triad region. Fluorescence of untargeted GCaMP6f was distributed throughout the muscle fibers and experienced large Ca²⁺-dependent changes, with obvious kinetic delays, upon application of voltage-clamp depolarizing pulses. Conversely, T306-GCaMP6f localized to the triad and generated Ca²⁺-dependent fluorescence transients of lower amplitude and faster kinetics for low and intermediate levels of Ca²⁺ release than those of untargeted GCaMP6f. By contrast, model simulation of the spatial gradients of Ca²⁺ following Ca²⁺ release predicted limited kinetic differences under the assumptions that the two probes were present at the same concentration and suffered from identical kinetic limitations. At the spatial level, T306-GCaMP6f transients within distinct regions of a same fiber yielded a uniform time course, even at low levels of Ca²⁺ release activation. Similar observations were made using GCaMP6f fused to the γ1 auxiliary subunit of Ca$_V$1.1. Despite the probe's limitations, our results point out the remarkable synchronicity of voltage-dependent Ca²⁺ release activation and termination among individual triads and highlight the potential of the approach to visualize activation or closure of single groups of RYR channels. We anticipate targeting of improved Ca²⁺ sensors to the triad will provide illuminating insights into physiological normal RYR function and its dysfunction under stress or pathological conditions.

Introduction

In skeletal muscle, there is molecular coupling between tetrads of Ca$_V$1.1 voltage-gated Ca²⁺ channels in the transverse tubule (t-tubule) membrane and every other RYR within the RYR channel arrays in the adjacent SR membrane. This constitutes the core machinery of excitation–contraction (EC) coupling. The functional outcome is that RYR-mediated SR Ca²⁺ release is triggered in response to Ca$_V$1.1 conformational changes generated by plasma membrane depolarization in a manner that is completely reversible upon t-tubule membrane repolarization. In terms of supporting structures, SR Ca²⁺ release takes place in a particular region called the triadic junction, where one t-tubule comes close (∼10 nm) to the RYR-loaded junctional membrane of two SR terminal cisternae (for review, see Rebbeck et al., 2014). Since the early 1980s, the physiological properties of voltage-activated RYR-mediated SR Ca²⁺ release in differentiated intact skeletal muscle fibers have essentially been studied by measuring cytosolic Ca²⁺ transients with diffusible Ca²⁺-sensitive dyes (e.g., Baylor et al., 1982; Palade and Vergara, 1982; Kovacs et al., 1983; Brum et al., 1988; Feldmeyer et al., 1990; Sárközi et al., 1996; Jacquemond, 1997; Woods et al., 2005; Hollingworth and Baylor, 2013; Braubach et al., 2014; Hernández-Ochoa et al., 2014; Manno et al., 2017). Over the years, this has provided detailed information regarding control of the activity of the RYR channel population in its native biological environment, and it has illuminated pathophysiological issues of EC coupling. In the mid-1990s, the advent of confocal imaging opened up a split between the frog (earlier gold-standard muscle preparation) and mammals. Indeed, the frog Ca²⁺ transient builds up on accumulation of local stereotyped elementary Ca²⁺ release events called Ca²⁺ sparks (Tsugorka et al., 1995; Klein et al., 1996) believed to result from mixed expression and function of the homologues of mammalian type 1

[1]Université Lyon, Université Claude Bernard Lyon 1, Centre National de la Recherche Scientifique UMR-5310, Institut National de la Santé et de la Recherche Médicale U-1217, Institut NeuroMyoGène, Lyon, France; [2]Departamento Nutrição, Universidade Federal de Pernambuco, Recife, Brazil; [3]Department of Physiology, Faculty of Medicine, University of Debrecen, Debrecen, Hungary.

Correspondence to Vincent Jacquemond: vincent.jacquemond@univ-lyon1.fr.

and type 3 RYR isoforms (Lai et al., 1992; Murayama and Ogawa, 1992). In contrast, these events are absent from mammalian muscle (Shirokova et al., 1998) where RYR3 expression is negligible (Flucher et al., 1999; Rossi et al., 2007). If one leaves aside the voltage-activated Ca²⁺ spark issue from RYR3-containing muscles, there are so far very limited experimental insights into the behavior of a single RYR1 channel or a single cluster of RYR1 channels during activation of intact differentiated mammalian muscle fibers. Confocal imaging of cytosolic Ca²⁺ in fibers from rat and mouse under conditions of low levels of voltage activation showed the presence of low-amplitude, long-lasting Ca²⁺ release events that were attributed to activation of either a single or a restricted number of highly synchronized RYR1 channels (Csernoch et al., 2004, 2008). Since then, no further experimental progress has been made that has increased our understanding of how single RYR1 channels or single clusters of coherently operating RYR1 channels open and close during t-tubule depolarization. This lack of information is even more arresting when compared with the substantial amount of literature concerning single-channel activity of RYR1 channels reconstituted in bilayer systems (for review, see Meissner, 2002; Laver, 2006), the relevance of which to the physiological situation remains questionable.

In an attempt to provide a deeper understanding of RYR1 function during muscle activity, we followed a strategy previously used in cardiac cells (Shang et al., 2014; Despa et al., 2014) consisting in targeting a Ca²⁺-sensitive probe to the junctional SR membrane. Indeed, having the probe in close vicinity to the RYRs was anticipated to provide a distinctive perspective view of channel activity during physiological SR Ca²⁺ release. For this, we expressed in muscle fibers GCaMP6f (Chen et al., 2013) fused either to a specific domain of the SR protein triadin (T306; Sanchez et al., 2018) or to the γ1 accessory partner of Ca$_V$1.1, and we tracked changes in triad-targeted GCaMP6f fluorescence triggered by voltage-clamp depolarizing pulses using confocal imaging. The affinity of GCaMP6f for Ca²⁺ is much too high to reliably track triadic Ca²⁺ changes during EC coupling activation. However, T306-GCaM6P was expected to tell us at least when, where, and for how long distinct RYR1 channels (or clusters of channels) of a same muscle fiber are activated at a given level of voltage activation. We compared the properties of macroscopic fluorescence transients from GCaMP6f and triad-targeted GCaMP6f and used model simulations to assess the consistency of the observations. We also looked for discrepancies in voltage-activated triad-targeted GCaMP6f signals between separate regions of a same muscle fiber during SR Ca²⁺ release activation. Results reveal that spatially distinct triadic regions exhibit remarkable uniformity in terms of onset and termination of Ca²⁺ release. They also offer first insights into what could represent local activity of a single group of RYR1s operating coherently. Although further developments and improvement will be needed to definitely assess the physiological gating behavior of single (or single groups of) RYR channels, the approach may prove to be precious for future understanding of healthy and diseased EC coupling function.

Materials and methods

All experiments and procedures were performed according to the ethics principles of the French Department of Veterinary Services and the French Ministry for Higher Education, Research, and Innovation, in accordance with the guidelines of the local animal ethics committee of the University Claude Bernard Lyon 1, the French Ministry of Agriculture (decree 87/848), and the revised European Directive 2010/63/EU. All experiments were performed at room temperature (20–22°C).

Plasmid constructs
pGP-CMV-GCaMP6f was a gift from Douglas Kim and the GENIE Project (Addgene; plasmid #40755; RRID: Addgene_40755). To trigger specific targeting of the biosensor to the triadic SR membrane, *GCaMP6f* cDNA was inserted into the modified pCMV vector, and its 3′ end was fused in frame to a sequence corresponding to a 16-amino-acid-long peptidic linker followed by the cDNA corresponding to residues 1–306 (T306) of human triadin. The pCMV vector was modified from pEGCP-N1 (Clontech) and contains the cytomegalovirus (CMV) promotor and 6xHIS, Xpress-tag, and T7 epitope tags located at the N terminus of the insert.

Alternatively, targeting of the biosensor to t-tubules was allowed by fusing in frame the cDNA sequence of mouse muscle dihydropyridine receptor γ1 subunit (Genscript; *Cacng1*) to the 5′ end of *GCaMP6f* cDNA in pcDNA3.1. Expression of the recombinant fusion biosensing protein was optimized by inserting a rigid peptidic linker, the so-called H4 linker (Amet et al., 2009), between the two protein domains. Final constructs were verified by DNA sequence analysis.

In vivo transfection
The experimental protocol for in vivo transfection was approved by the Animal Experimentation Committee (#C2EA-15) of the Rhône-Alpes Region and the French Ministry for Higher Education, Research, and Innovation. Expression in mouse flexor digitorum brevis and interosseus muscles was achieved by plasmid injection and subsequent electroporation following previously described procedures (Lefebvre et al., 2011). In brief, 8–16-wk-old Swiss OF1 male mice were used. Mice were anesthetized by isoflurane inhalation using a commercial delivery system (Univentor; Univentor 400 Anesthesia Unit), and a 20 μl volume of a solution containing 2 mg/ml hyaluronidase dissolved in sterile saline was injected into the footpads of each hindpaw of the animal. Mice were reanesthetized 1 h later and a volume of 20 μl of a solution containing 30–50 μg plasmid DNA diluted in NaCl 0.9% was injected into the footpads. Two gold-plated stainless steel acupuncture needles connected to the electroporation apparatus were then inserted under the skin, near the proximal and distal portion of the foot, respectively. The electroporation protocol consisted of 20 pulses of 130 V/cm amplitude and 20 ms duration delivered at a frequency of 2 Hz by a BTX ECM 830 square-wave pulse generator (Harvard Apparatus). Isolation of muscle fibers and experimental observations and measurements were performed 7–8 d later. In one set of experiments, muscles from a mouse were electroporated with the T306-GCaMP6f construct together with a

Sanchez et al.
Triadic Ca²⁺ changes in skeletal muscle

Journal of General Physiology 2 of 20
https://doi.org/10.1085/jgp.202012592

plasmid encoding mRFP-tagged junctophilin 1 (provided by V. Sorrentino, University of Siena, Siena, Italy).

Preparation of isolated muscle fibers
Single fibers were isolated from the transfected muscles using a previously described procedure (Jacquemond, 1997). Briefly, mice were anaesthetized by isoflurane inhalation and then killed by cervical dislocation before removal of the muscles. Muscles were incubated in Tyrode solution containing collagenase (Sigma; type 1) for 60 min at 37°C. Single fibers were then obtained by mechanical trituration of a given muscle within a 50-mm-wide culture μ-dish (ibidi) filled with culture medium containing 10% FBS (Eurobio; MI199), the bottom of which had been first coated with a thin layer of silicone. Fibers were embedded within silicone so that only a portion of the fiber extremity remained out, in contact with the extracellular medium. In the case of fibers expressing T306-GCaMP6f, care had to be taken to ascertain that the fiber portion left out of the silicone did exhibit expression of the probe.

Electrophysiology
Voltage clamp was achieved with a micropipette filled with a solution mimicking the composition of the intracellular medium (see Solutions). The tip of the pipette was inserted into the silicone-insulated part of the fiber. To ease intracellular dialysis and reduce series resistance, the tip was gently crushed against the bottom of the chamber. In the most routine experimental conditions, the pipette solution contained no exogenous Ca^{2+} buffer and contraction was blocked by using N-benzyl-p-toluene sulfonamide (BTS) in the extracellular solution (see Solutions), which weakens interaction of myosin with actin (Cheung et al., 2002). In some experiments, the pipette solution also contained rhod-2 (see Solutions), and in such cases the fiber interior was dialyzed for a period of 30 min to allow for intracellular equilibration of the solution. The chlorided silver wire inside the pipette was connected to an RK-400 patch-clamp amplifier (Bio-Logic) used in whole-cell voltage-clamp configuration, in combination with an analogue-digital converter (Axon Instruments; Digidata 1440A) controlled by pClamp 9 software (Axon Instruments). Analogue compensation was adjusted to further decrease the effective series resistance. The holding voltage was set to −80 mV.

Confocal imaging
Confocal imaging of fibers expressing GCaMP6f and T306-GCaMP6f was conducted with a Zeiss LM5 Exciter microscope equipped with a 63× oil-immersion objective (NA, 1.4). In routine conditions, GCaMP6f was excited with the 488-nm line of an argon laser and a 505-nm-long pass filter was used on the detection channel. In fibers dialyzed with rhod-2, a 505–530-nm bandpass filter was used for GCaMP6f fluorescence detection. Rhod-2 excitation was from the 543-nm line of a HeNe laser, and rhod-2 fluorescence was collected above 560 nm. GCaMP6f and rhod-2 Ca^{2+} transients were imaged using the line-scan mode (x,t) of the system with the line parallel to the longitudinal axis of the fibers. Images were taken with a scanning frequency ranging from 1.15 to 7.7 ms per line. The length of the scanned

line was 51 μm. Slow scanning was used to reduce the signal to noise ratio. Confocal imaging of fibers expressing $γ_1$-GCaMP6f was conducted with an upgraded version (LSM-800) of the microscope equipped with the same 63× oil-immersion objective. $γ_1$-GCaMP6f fluorescence was excited with a 488-nm diode laser. Unless otherwise specified, images were taken with a scanning frequency of either 0.91 or 4.95 ms per line. Fluorescence changes were expressed as F/F_0, where F_0 is the baseline fluorescence. In some cases, the spontaneous decrease in fluorescence due to photobleaching was corrected for by using a single- or two-exponential fit to the portion of F/F_0 trace before and after a pulse was applied and extrapolating the fit to the entire trace duration. Some of the traces shown were smoothed using a simple rolling average. In all graphs presenting fluorescence transients, the y scale bar corresponds to the indicated multiple or fraction of the baseline fluorescence F_0. The rise time of the fluorescence transients was quantified from the time elapsed between the beginning of the pulse and either the peak of the transient (time to peak) or 80% of the peak of the transient ($t_{80\%}$). The rate of decay of the F/F_0 fluorescence transients was quantified by fitting a single exponential function, starting 20–50 ms after the end of the pulse.

Calibration
To calibrate the response of T306-GCaMP6f, isolated muscle fibers expressing the probe were permeabilized with 0.05% saponin in the presence of a solution containing (in mM) 140 KCl, 10 EGTA, 5 PIPES, 0.05 BTS, and 2 2,3-butanedione monoxime. Permeabilized fibers were then fully embedded into silicone grease and successively dialyzed, each time for 30 min, with a version of the above solution differing by the concentration of total added calcium (from 0 to 11 mM). Dialysis of each solution was achieved through a distinct micropipette, the blunt tip of which was inserted into the silicone-embedded muscle fiber. A confocal image of T306-GCaMP6f fluorescence was taken at the beginning of the experiment and after each dialysis period (Fig. 1 B). All solutions were equilibrated at pH 7.00. The free calcium concentration in each solution was calculated using MaxChelator (C. Patton, Stanford University, Stanford, CA).

Simulation of calcium movements in the presence of either GCaMP6f or T306-GCaMP6f
The simulation program was written in VisualStudio (Microsoft) and ran as an executable file (EXE) after compilation on standard desktop computers. The spatial positions were subdivided into three categories, namely (1) the triadic junction, where only the dye and the release channels were present; (2) the area around the terminal cisternae, where the dye and the SERCA pump were present; and (3) the bulk myoplasmic space, where both the nontargeted dye (if the dye was targeted, it was assumed not to be present in this compartment), the SERCA pump, and the calcium buffers (troponin and parvalbumin) were present. A voxel map to illustrate this is presented in Fig. S1.

First, the rate of calcium release from the SR (dR/dt) during a depolarizing pulse was calculated. It was assumed to activate
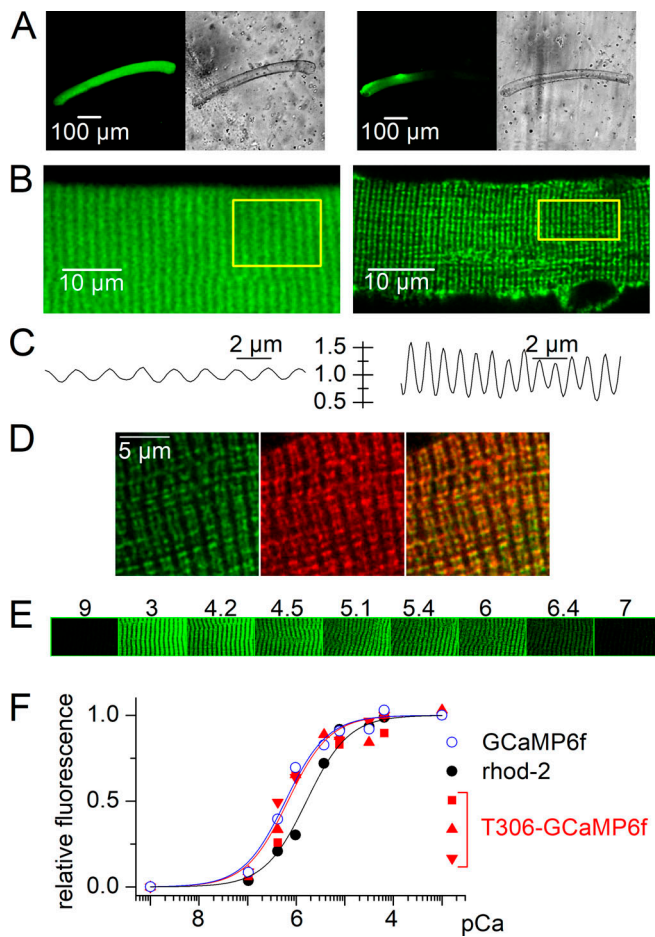
Sanchez et al.
Triadic Ca^{2+} changes in skeletal muscle

Journal of General Physiology 3 of 20
https://doi.org/10.1085/jgp.202012592

Figure 1. **Expression pattern and Ca²⁺ sensitivity of GCaMP6f and T306-GCaMP6f.** **(A)** Illustrative examples of the global and patchy expression patterns of GCaMP6f (left) and T306-GCaMP6f (right) in muscle fibers, respectively. **(B)** Typical subcellular fluorescence pattern of GCaMP6f (left) and T306-GCaMP6f (right) in muscle fibers. **(C)** Fluorescence profile along the main axis of the muscle fibers within the box-highlighted region in the above-corresponding image in B. The y scale corresponds to the background-corrected fluorescence intensity normalized by the mean intensity of the profile. **(D)** Confocal frames from a muscle fiber coexpressing T306-GCaMP6f (green channel) and mRFP-tagged junctophilin 1 (red channel). The right panel shows the overlay. **(E)** Confocal fluorescence images from a T306-GCaMP6f expressing muscle fiber upon equilibration with solutions of varying pCa (−log [Ca²⁺]; above indicated values). **(F)** Ca²⁺ dependence of the relative change in fluorescence in three fibers expressing T306-GCaMP6f (red filled squares and triangles), one fiber expressing GCaMP6f (open blue circles), and droplets of calibrating solutions containing rhod-2 (filled black circles). Superimposed colored curves show the corresponding results from fitting a Hill equation. See Materials and methods for details.

and then partially inactivate, following a single exponential time course for both, with time constants (τ_a and τ_i, respectively) adjusted to represent the voltage dependence measured under experimental conditions:

$$\frac{dR}{dt} = R_{max} \cdot \left(1 - e^{-\frac{t}{\tau_a}}\right) \cdot \left(e^{-\frac{t}{\tau_i}} + Sl\right) \cdot \left(Ca_{SR} - R(t)\right) \bigg/ Ca_{SR}, \quad (1)$$

where R_{max} is the theoretical maximum, Sl is the noninactivating component of dR/dt at the given voltage, $R(t)$ is the amount of calcium released until time t $\left(i.e., \ R(t) = \int_0^t \frac{dR}{dy} dy\right)$, and Ca_{SR} is

the SR calcium content at $t = 0$. Four sets of parameters were used to generate four sets of Ca²⁺ input release fluxes recapitulating basic properties of physiological SR Ca²⁺ release generated by 0.5-s-long voltage-clamp depolarizing pulses of increasing amplitude (referred to as 1–4 in Fig. 8). For this, we used values for R_{max}, Sl, τ_a, and τ_i of 1, 7, 10, and 30 µM.ms⁻¹; 0.2, 1.4, 2, and 6 µM.ms⁻¹; 200, 30, 8, and 5 ms; and 10,000, 22, 20, and 2 ms for input fluxes 1–4, respectively. Upon repolarization, dR/dt was assumed to return to its resting value (Leak), again following a single exponential:

$$\frac{dR}{dt} (t > t_{pulse}) = \frac{dR(t = t_{pulse})}{dt} \cdot e^{\left\{\frac{-(t - t_{pulse})}{\tau_r}\right\}} + Leak, \quad (2)$$

where t_{pulse} is the time when the depolarizing pulse ends and τ_r is the time constant of the decline, which was set to 2 ms for all simulations, as the repolarization was to −80 mV (the holding potential) in all cases.

Note that Eq. 1 incorporates the depletion of calcium in the SR as the release waveform is scaled by the term $(Ca_{SR} - R(t))/Ca_{SR}$, which corresponds to the relative amount of Ca²⁺ remaining in the SR at time t, which is the relative driving force for Ca²⁺. Leak was set to be equal to the amount of calcium transported by the SR calcium pump into the SR at resting conditions.

To follow the movement of the released calcium, the myoplasmic space was subdivided into equal-sized voxels of 10³ nm³. The change in the calcium concentration ($\partial[Ca]/\partial t$) in a voxel was calculated as

$$\frac{\partial[Ca]}{\partial t} = D \frac{\partial^2[Ca]}{\partial x^2} - \sum_i \frac{d[Ca - X_i]}{dt} - P, \quad (3)$$

where D is the diffusion coefficient for Ca²⁺ in the myoplasm, [Ca − X_i] is the amount of calcium bound to X_i, and P is the amount transported by the SR calcium pump in a given time. X_i represents the different calcium binding sites in the muscle (troponin C, parvalbumin, and the SR calcium pump) and either GCaMP6f or T306GCaMP6f. In terms of diffusion, as the targeted probe, troponin, and the SERCA pump are immobile, the only buffers that could be considered are parvalbumin and the nontargeted probe. As the diffusion coefficient depends on the molecular weight (size) of the diffusing particle (using the Stokes–Einstein equation and assuming that the particle is close to a sphere, this gives that $D \sim M^{-1/3}$), the diffusion coefficients of parvalbumin and of the dye would be 8–20 times smaller than that of Ca²⁺, and therefore, their diffusion was neglected in the simulations.

All binding sites were assumed to follow first order binding kinetics. Equations used to calculate Ca²⁺ binding and Ca²⁺ removal were as described by Brum et al. (1988). For troponin C and parvalbumin binding sites, we used parameter values from Baylor and Hollingworth (2003) for fast-twitch mouse muscle fibers, with values for all rate constants increased 1.5-fold to account for the difference in temperature (16°C versus 22°C in our conditions), and with the concentration of parvalbumin binding sites decreased 1.4-fold to account for the reported difference between extensor digitorum longus and flexor digitorum brevis muscles (Raymackers et al., 2000). For troponin C binding sites, this corresponded to a total concentration of

Sanchez et al.
Triadic Ca²⁺ changes in skeletal muscle

Journal of General Physiology 4 of 20
https://doi.org/10.1085/jgp.202012592

240 µM, a K_d of 1.3 µM and on and off rate constants of 0.13 µM^{-1}.ms^{-1} and 0.17 ms^{-1}, respectively. For Ca-Mg binding sites on parvalbumin, this corresponded to a total concentration of 1,071 µM; a K_d and on and off rate constants for Ca^{2+} binding of 12 nM, 0.063 µM^{-1}.ms^{-1}, and 7.5 × 10^{-4} ms^{-1}, respectively; and a K_d and on and off rate constant for Mg^{2+} binding of 91 µM, 4.95 × 10^{-5} µM^{-1}.ms^{-1} and 4.5 × 10^{-3} ms^{-1}, respectively. Calcium transport across the SR membrane was included with a rate assumed to be proportional to the fractional occupancy of the SR pump sites with a site concentration of 200 µM and a K_d of 1 µM (Garcia and Schneider, 1993). Values for maximum pump rate and on and off rate constants of Ca^{2+} binding were assumed to be 10 µM.ms^{-1}, 0.16 µM^{-1}.ms^{-1}, and 0.16 ms^{-1}, respectively. For Ca^{2+} binding to GCaMP6f, unless otherwise indicated, binding site concentration, K_d, and on and off rate constants were assumed to be 100 µM, 0.65 µM, 0.0185 µM^{-1}.ms^{-1}, and 0.012 ms^{-1}, respectively. Changing the concentration of the triad-targeted probe (T306-GCaMP6f) within the 10–1,000 µM range negligibly affected the size and shape of the modeled Ca^{2+} transients. When including Ca^{2+} binding to EGTA in the simulation, EGTA was assumed to be present at a concentration of 7.2 mM, and values for K_d and on and off rate constants were assumed to be 36 nM, 0.056 µM^{-1}.ms^{-1}, and 0.002 ms^{-1}, respectively (Schuhmeier et al., 2003). The Ca^{2+} diffusion coefficient D was assumed to be 0.53 µm^2.ms^{-1} (Donahue and Abercrombie, 1987). Resting [Ca^{2+}] and [Mg^{2+}] were assumed to be 0.05 µM and 1 mM, respectively. The initial SR concentration was assumed to be 2 mM.

Note that in Eq. 1, a one-dimensional diffusion was assumed. This simplification was justified by selecting the number of voxels (N_i) at a given distance (x_i) to be dependent on i ($i = 1,... 50$), i.e., $i = 1$ represented the junctional space and $i = 50$ the middle of the sarcomere, with N_1 being the smallest and N_{50} the largest of all N_i's. Due to morphological restraints and inherent symmetry in the architecture of the muscle fiber, diffusion was considered only in one direction (toward the middle of the sarcomere), and boundary conditions for [Ca^{2+}] were set as to reflect this symmetry.

Voxels at a given distance (corresponding to the same x_i) were assumed to behave identically in terms of their calcium handling properties. The following different possibilities of calcium movements for any voxel were considered: (1) calcium release from the SR can occur (only for $i = 1$), (2) the dye is present, (3) SR calcium pump is present, and (4) other calcium binding sites (X_i) are present. The model thus inherently accounted for the differences in binding and transport at different positions and different time points, since the calcium concentration is a function of space and time. For instance, calcium binding to the SERCA pump was calculated for each and every voxel where the pump was assumed to be present (which corresponded to every voxel except those into which Ca^{2+} release occur), and the transport was then calculated using the appropriate equation. The implementation allowed the user to change the behavior of any voxel in this respect, which permitted us to study, for instance, the cases of targeted and nontargeted dye.

Solutions
The standard extracellular solution used for voltage clamp contained (in mM) 140 TEA-methanesulfonate, 2.5 CaCl$_2$, 2 MgCl$_2$, 1 4-aminopyridine, 10 HEPES, 0.002 tetrodotoxin, and 0.05 BTS. The standard intrapipette solution contained (in mM) 130 K-glutamate, 5 Na$_2$-ATP, 5 Na$_2$-phosphocreatine, 5.5 MgCl$_2$, 5 glucose, 5 HEPES, and, in some experiments, 0.1 rhod-2. In some experiments, the extracellular solution contained no BTS while the intracellular solution also contained 15 mM EGTA and 6 mM CaCl$_2$. All solutions were adjusted to pH 7.20.

Statistics
Statistical analysis was performed with Origin 8.0. Least-squares fits were performed using a Marquardt–Levenberg algorithm routine included in Microcal Origin (OriginLab). Data values are presented as means ± SEM for n fibers. Statistical significance was determined using a Student's t test (*, $P \le 0.05$; **, $P \le 0.01$; ***, $P \le 0.001$).

Online supplemental material
Fig. S1 shows a voxel map illustrating the distribution of the spatial positions used in the model simulations. Fig. S2, Fig. S3, and Fig. S4 show results from the same simulations as Fig. 6, Fig. 7, and Fig. 8, respectively, with the value for the Ca^{2+} diffusion coefficient being reduced from 0.53 µm^2.ms^{-1} to 0.02 µm^2.ms^{-1}.

Results
Expression pattern and Ca^{2+} sensitivity of T306-GCaMP6f
The fluorescence pattern of muscle fibers expressing GCaMP6f and T306-GCaMP6f substantially differed (Fig. 1, A and B). GCaMP6f fluorescence was distributed throughout the entire volume of the muscle fibers and either yielded no specific subcellular features or, as shown in Fig. 1, B and C (left), a faint transversally striated pattern with a spatial period of ~2 µm. In our experience, this can occasionally be observed with diffusible dyes or expressed proteins and likely results from unspecific accumulation/binding to proteins at the Z line, thus making the longitudinal fluorescence pattern yield a spatial period analogous to the sarcomere length. In contrast, muscle fibers expressing T306-GCaMP6f exhibited one or a few restricted areas of elevated fluorescence (Fig. 1 A, right). Within each of these spots, the fluorescence intensity peaked according to a transversally striated pattern with a spatial period of 1 µm (Fig. 1, B and C, right). Because there are two t-tubule–SR junctions per sarcomere, each at the intersection between the A band and the I band, this is consistent with expression at the triad, either in the t-tubule membrane or in the junctional SR membrane (Sorrentino, 2011; Barone et al., 2015). However, the combination of the two features (local spots, 1-µm-spaced striations) is reminiscent in this same system of either RYR expression (Legrand et al., 2008; Lefebvre et al., 2011) or expression of T306 fused with various voltage-sensitive fluorescence probes, which we proved localized at the SR membrane (Sanchez et al., 2018). Thus, this is one encouraging piece of evidence that, in the present case, the T306 sequence was effective in targeting the probe to the expected location. Further evidence for triadic localization is also illustrated in Fig. 1 D, which shows colocalization between T306-GCaMP6f and

mRFP-tagged junctophilin 1, an archetypal triadic protein (e.g., Rossi et al., 2019).

Purified GCaMP6f was reported to exhibit a K_d for Ca^{2+} of ~0.38 µM (Chen et al., 2013), whereas a value of 0.63 µM was reported from in situ calibration of GCaMP6f fused with triadin or junctin expressed in cardiac cells (Shang et al., 2014). In our conditions, calibration of T306-GCaMP6f fluorescence was achieved in situ in three muscle fibers by successively equilibrating the cytosolic compartment with solutions containing different levels of free calcium using the procedure described in Materials and methods. An example of T306-GCaMP6f fluorescence images collected under these conditions is shown on top of Fig. 1 E, while fluorescence values normalized to the minimum (F_{min}) and maximum fluorescence (F_{max}) in each fiber are reported with filled red square and triangle symbols in Fig. 1 F. Fitting the data with a Hill equation gave a mean K_d value of 0.65 ± 0.05 µM and a Hill coefficient of 1.17 ± 0.13 (red curve). The mean value for the ratio F_{max}/F_{min} from these three fibers and from two additional fibers challenged only by the two extreme Ca^{2+} concentrations was 11.0 ± 0.9. Fig. 1 F also shows fluorescence values from one GCaMP6f-expressing fiber that we could successfully equilibrate in the presence of ionomycin with the same calibration solutions (open blue circles). The superimposed blue curve corresponds to the result from the fit which gave a K_d of 0.60 µM and a Hill coefficient of 1.1, thus very similar to the T306-GCaMP6f data. However, the F_{max}/F_{min} value from this fiber was 57, substantially larger than the above T306-GCaMP6f mean value but similar to the value reported in vitro (~52; Chen et al., 2013). We took this as a first indication that the dynamic range of the T306-GCaMP6f response is reduced as compared with that of GCaMP6f. The graph in Fig. 1 F also shows results from rhod-2 fluorescence calibration in droplets with the same solutions, from which fitting a 1:1 binding curve gave a K_d of 1.63 µM (black curve). Altogether, these results are consistent with T306-GCaMP6f being present in the triadic SR membrane and exhibiting an affinity for Ca^{2+} similar to that of free GCaMP6f.

Kinetic limitations of GCaMP6f and T306-GCaMP6f

Although the sensitivity and speed of response of genetically engineered Ca^{2+}-sensitive probes have been improved over the years (e.g., Chen et al., 2013), it was important to quantify how GCaMP6f compares to a commonly used synthetic indicator, in our conditions. Fig. 2 A shows fluorescence transients triggered by large voltage-clamp depolarizing pulses of 5, 10, 20, and 50 ms duration, evoking maximal SR Ca^{2+} release, in a fiber expressing GCaMP6f and dialyzed with rhod-2. Transients were calculated by averaging fluorescence over the entire scanned line. The two probes generated fluorescence transients of similar F/F_0 maximal amplitude but the overall time course of GCaMP6f transients (thick blue traces) clearly lagged behind that of rhod-2 (thin black traces), as also shown from the mean values for time to peak and time constant of decay of the fluorescence transients from three fibers tested in the same conditions (graphs at the bottom). Pairs of traces shown in Fig. 2 B were obtained in the same experimental conditions but from a fiber challenged by voltage pulses of increasing amplitude. Again,

there is a considerable delay in the GCaMP6f response as compared with that of rhod-2. This is particularly dramatic for the low levels of SR Ca^{2+} release activation for which GCaMP6f barely detects the fast early Ca^{2+} rise seen by rhod-2 and keeps rising at times where rhod-2 has reached a more or less steady level. This time-course distortion is due to the known slow kinetics of the GCaMP probes. Although a complex kinetic model would be necessary to strictly account for the kinetic steps of the Ca^{2+}-GCaMP reaction (e.g., Helassa et al., 2015), we resumed it to a simple binding equilibrium, and we adjusted the GCaMP6f rate constants values to best match the rhod-2 and GCaMP6f calculated Ca^{2+} signals.

$Ca^{2+}(t)$ was calculated from fluorescence ($F(t)$) following the principles described by Sztretye et al. (2011):

$$Ca^{2+} = \frac{k_{off} \ (F - Fmin) + \frac{dF}{dt}}{k_{on}(Fmax - F)}.$$

For rhod-2, we used a k_{off} value of 0.13 ms^{-1} (Sztretye et al., 2011) and a value for k_{on} so that K_d equals 1.63 µM. For GCaMP6f, the calibration value of 0.65 µM for K_d was used and values for k_{on} and k_{off} were adjusted. For both rhod-2 and GCaMP6f, values for F_{max}/F_{min} (ratio of fluorescence in saturating Ca^{2+} to the corresponding value in absence of Ca^{2+}) were also adjusted. The inset in Fig. 2 A shows the superimposed changes in free Ca^{2+} calculated from rhod-2 (thin black traces) and GCaMP6f (thick blue traces) in response to the 5- and 20-ms-long pulses. Transients were calculated with values for F_{max}/F_{min} of 27 and 42 for rhod-2 and GCaMP6f, respectively, and with GCaMP6f k_{on} and k_{off} values of 0.018 $µM.ms^{-1}$ and 0.012 ms^{-1}, respectively. In the two other fibers tested in these same conditions a similar reasonable consistency between the calculated rhod-2 and GCaMP6f Ca^{2+} transients was obtained with the same values for the rate constants and for the GCaMP6f F_{max}/F_{min} value, provided that some adjustment was made for rhod-2 F_{max}/F_{min}. Thus, 2 times and 10 times lower association and dissociation rate constants for GCaMP6f than for rhod-2, respectively, appear to reasonably account for the Ca^{2+} binding kinetics of GCaMP6f.

Fig. 3 presents a set of data equivalent to the one in Fig. 2 A but from fibers expressing T306-GCaMP6f. As was the case for the nontargeted version of the probe, T306-GCaMP6f transients (thick red traces) exhibited a slower time course than the simultaneously detected rhod-2 transients (thin black traces), with larger values for the time to peak and time constant of decay of the transients (Fig. 3, bottom graphs). The peak amplitude of the F/F_0 rhod-2 transients in this series of experiments was smaller than in the parallel series of experiments in fibers expressing GCaMP6f (Fig. 2). The reason for this is unclear and may be related to the fact that resting rhod-2 fluorescence in these experiments tended to increase with time, raising doubt as to whether the rhod-2 F_0 level was reliable. We do not exclude that an interaction between rhod-2 and the probe may underlie this effect. The peak amplitude of the T306-GCaMP6f transients was smaller than that of the GCaMP6f transients, and this was a consistent feature throughout all experiments, likely resulting, at least in part, from its reduced dynamic range.

To test whether expression of the probe may have affected SR Ca^{2+} release, we compared transients at two locations of a fiber
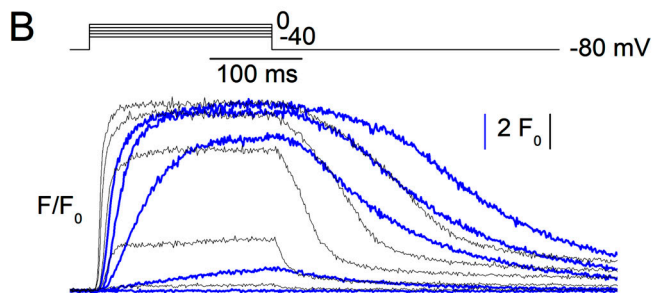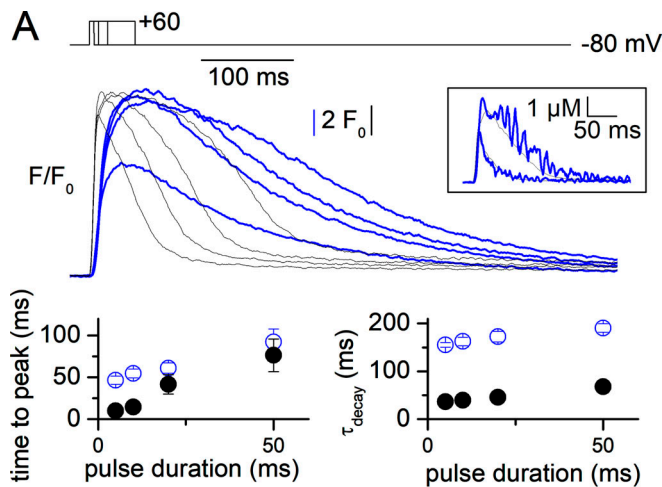
Figure 3. **Kinetic features of T306-GCaMP6f Ca²⁺ transients elicited by short depolarizing pulses.** Simultaneous T306-GCaMP6f (thick red traces) and rhod-2 (thin black traces) fluorescence transients detected from a muscle fiber in response to the depolarizing pulse protocol shown on top. The respective T306-GCaMP6f and rhod-2 fluorescence transients are shown scaled to a similar peak amplitude, with corresponding red and black y scale bars both indicating a fluorescence change of $0.5 \times F_0$. The two graphs at the bottom report mean values for the time to peak F/F_0 and for the time constant of F/F_0 decay (τ_{decay}) after repolarization, from four fibers expressing T306-GCaMP6f, loaded with rhod-2, and stimulated with the same voltage-clamp protocol. Filled black circles and open red circles correspond to measurements from rhod-2 and T306-GCaMP6f transients, respectively. Vertical bars represent the SEM.

Figure 2. **Kinetic features of GCaMP6f Ca²⁺ transients. (A)** Simultaneous GCaMP6f (thick blue traces) and rhod-2 (thin black traces) fluorescence transients detected from a muscle fiber in response to the voltage-clamp protocol shown on top, consisting of pulses to +60 mV of 5, 10, 20, and 50 ms duration. The respective GCaMP6f and rhod-2 fluorescence transients are shown scaled to a similar peak amplitude, with corresponding blue and black y scale bars both indicating a fluorescence change of $2 \times F_0$. The inset on the right shows the kinetically corrected Ca²⁺ transients calculated from the GCaMP6f and rhod-2 traces elicited by the 5-ms-long pulse and by the 20-ms-long pulse (see text for details). The two graphs at the bottom report mean values for the time to peak F/F_0 and for the time constant of F/F_0 decay (τ_{decay}) after repolarization, from three fibers expressing GCaMP6f, loaded with rhod-2, and stimulated with the same voltage-clamp protocol. Filled black circles and open blue circles correspond to measurements from rhod-2 and GCaMP6f transients, respectively. Vertical bars represent the SEM. **(B)** Illustrative example of simultaneously detected GCaMP6f (thick blue traces) and rhod-2 (thin black traces) Ca²⁺ transients in response to 200-ms-long depolarizing pulses of increasing amplitude.

exhibiting a strong gradient of T306-GCaMP6f expression. Fig. 4 A shows the T306-GCaMP6f (left, red) and rhod-2 (right, black) resting fluorescence intensity profile along the scanned line. Despite the noise in the fluorescence along one scanned line, a succession of double peaks every 2 µm is clearly visible in the T306-GCaMP6f profile, showing evidence of triadic localization. It is noticeable that this double-peak pattern (as also observed in Fig. 14 A) is more pronounced than in Fig. 1 B, where successive double peaks are not well separated by a region of lower fluorescence. The pronounced double-peak pattern is indicative of a shorter distance between t-tubules on each side of the Z line than between t-tubules on each side of the A-I junction. We are not completely sure of the reason for this variability of the
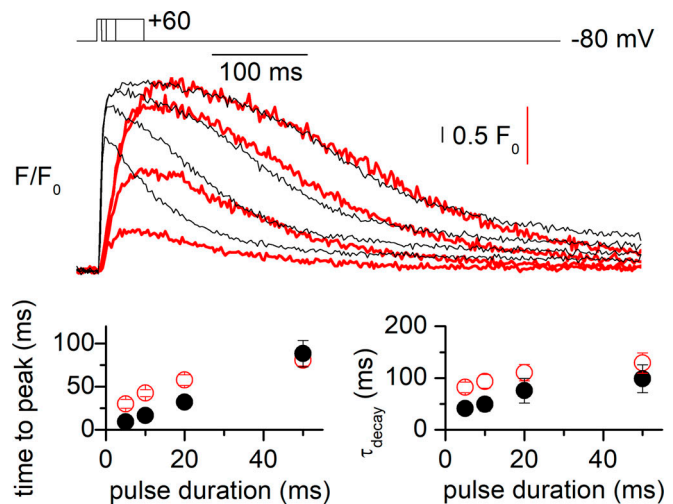
triadic pattern. Although never pinpointed, it is present in the literature and may be related to subtle differences in muscle fiber resting state and/or sarcomere length. Fig. 4 B shows the T306-GCaMP6f (left, red) and rhod-2 (right, black) fluorescence transients measured in response to a pulse from −80 to −10 mV in the high-expression region of the line. The superimposed gray trace in each panel shows the corresponding signal measured simultaneously in the lower expression region of the line. The high- and low-expression line regions over which fluorescence transients were averaged are indicated by horizontal bars at the bottom of Fig. 4 A. Despite an approximately five-times difference in the resting level (F_0) of T306-GCaMP6f fluorescence between the two regions of the line, both the rhod-2 and the T306-GCaMP6f F/F_0 transients were similar, providing no indication that probe expression/overexpression strongly affects SR Ca²⁺ release. Such a comparison was made in six fibers exhibiting a spatial gradient of resting T306-GCaMP6f fluorescence with a ratio of maximal to minimal fluorescence between 2 and 9 along the scanned line. There was no reproducible trend of difference in the peak amplitude of the T306-GCaMP6f and rhod-2 F/F_0 transients between regions of a same fiber yielding high and lower levels of T306-GCaMP6f, respectively. On average, the ratio of peak amplitude T306-GCaMP6f and rhod-2 F/F_0 transients in the high-expression region to the corresponding values in the low-expression region along a 50- to 100-µm-long scanned line was 0.93 ± 0.1 and 0.90 ± 0.1, respectively.
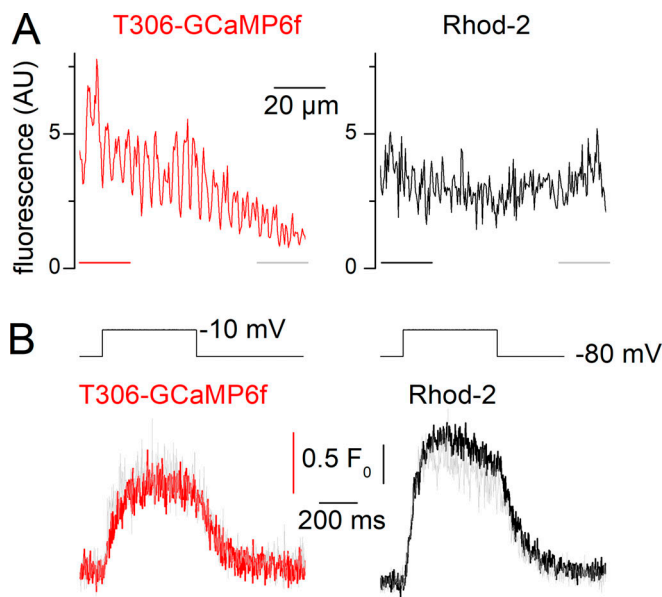
Figure 4. **Ca²⁺ transients within a muscle fiber region exhibiting a gradient of T306-GCaMP6f expression. (A)** T306-GCaMP6f (red trace) and rhod-2 (black trace) distribution along a line scanned in a fiber region exhibiting a T306-GCaMP6f gradient of expression. **(B)** Voltage-activated T306-GCaMP6f and rhod-2 transients recorded within the high- (red and black traces in the left and right panel, respectively) and low-expression region (superimposed gray traces) of T306-GCaMP6f. The high- and low-expression line regions over which fluorescence transients were averaged are indicated by horizontal colored (red or black) and gray lines, respectively, at the bottom of the fluorescence distribution profiles in A. AU, arbitrary units.

Voltage-dependent GCaMP6f and T306-GCaMP6f Ca²⁺ transients

Comparing the response of the free and triad-targeted probes to different levels of SR Ca²⁺ release activation was expected to provide further insights into the changes in Ca²⁺ experienced by the two probes. This was made in the absence of rhod-2, using 500-ms-long pulses to different voltage levels. Fig. 5 shows representative transients from the two probes, still elicited in the presence of extracellular BTS. For such long pulses, the presence of BTS was not sufficient to completely block contraction at large depolarizing voltage levels. For this reason, most measurements were taken with pulses up to values rarely exceeding −10 mV. GCaMP6f and T306-GCaMP6f transients looked similar, and there was no stringent qualitative feature that would irrefutably allow identification of which transients corresponded to which probe. Quantitative features were compared in a few fibers of each group that were all stimulated by pulses to −30, −25, −20, and −15 mV and for which there was no indication of fiber movement. There were quantitative differences between the two series: T306-GCaMP6f transients exhibited F/F_0 peak amplitude values substantially smaller than those of GCaMP6f transients (Fig. 5 B, left). The rate of rise, estimated from the time to reach 80% of the peak fluorescence, was faster for T306-GCaMP6f transients at the low values of voltage activation (Fig. 5 B, middle). The time constant of T306-GCaMP6f fluorescence decay after the end of the

pulses exhibited values twice smaller than those from GCaMP6f transients (Fig. 5 B, right).

Model simulation of the changes in Ca²⁺ and of the corresponding GCaMP6f response, from the triadic space to the center of the sarcomere

The above results show that following SR Ca²⁺ release, GCaMP6f and T306-GCaMP6f generate fluorescence changes with a qualitatively similar time course, a feature that was not intuitively expected considering that the targeted probe should experience much larger changes in Ca²⁺ concentration than the bulk (e.g., Pape et al., 1995). To quantitatively explore this issue and determine whether the differences (or absence of differences) between the signals from the two probes are consistent, we made model simulations of the changes in free Ca²⁺ and in corresponding Ca–probe complexes occurring along a quarter of sarcomere distance from the Ca²⁺ release site. The model was implemented as described in Materials and methods. Ca²⁺ binding to both GCaMP6f and triad-targeted GCaMP6f (referred to as T306-GCaMP6f for simplicity) was assumed to occur with the rate constants found to match the GCaMP6f and rhod-2 Ca²⁺ transients (Fig. 2 A). Because of the difference (and related uncertainty) regarding the dynamic range of the two probes, only the predicted time courses of change in Ca-bound GCaMP6f and in Ca-bound triad-targeted GCaMP6f were compared. Fig. 6 illustrates the model predictions in response to a small Ca²⁺ release (peak value of 1.5 μM.ms⁻¹; Fig. 6 A). The images in Fig. 6, B and D, show the calculated change in free Ca²⁺ along a 0.5-μm distance from the release site (top) in the presence of GCaMP6f or T306-GCaMP6f, respectively, while images in Fig. 6, C and E, show the corresponding changes in Ca²⁺ bound to each of the two probes. The three superimposed traces below each image show the corresponding maximum change (at the release site, thick red trace), minimum change (0.5 μm away/mid-sarcomere, thin blue trace), and the average change (dotted black trace), which would correspond to the experimentally detected signal. In each panel, the straight dashed line at the bottom corresponds to the zero level. Results show that despite a very substantial gradient of Ca²⁺ change along the distance from the release site, the average time course of Ca²⁺ bound to the probe did not stringently differ between the targeted and the nontargeted version of the probe. An identical representation of the predictions made in response to a strong SR Ca²⁺ release flux (peak value of 31.6 μM.ms⁻¹) is shown in Fig. 7, from which the same conclusions could be drawn. Indeed, despite a 10-fold difference in peak Ca²⁺ between the release site and the mid-sarcomere region, the average time course of Ca²⁺ bound to GCaMP6f and triad-targeted GCaMP6f was similar. Comparison between the predicted time course of Ca²⁺ bound to the two probes is more explicitly made in Fig. 8, which shows the average changes in response to four different SR Ca²⁺ release input fluxes of distinct peak amplitude and waveform (labeled 1–4; Fig. 8 A). Fig. 8 B shows the corresponding absolute average changes in Ca-GCaMP6f (left, blue) and Ca-T306-GCaMP6f (right, red), while Fig. 8 C shows the same changes in Ca-GCaMP6f and Ca-T306-GCaMP6f after normalization, superimposed for each release flux condition. Values for the time to
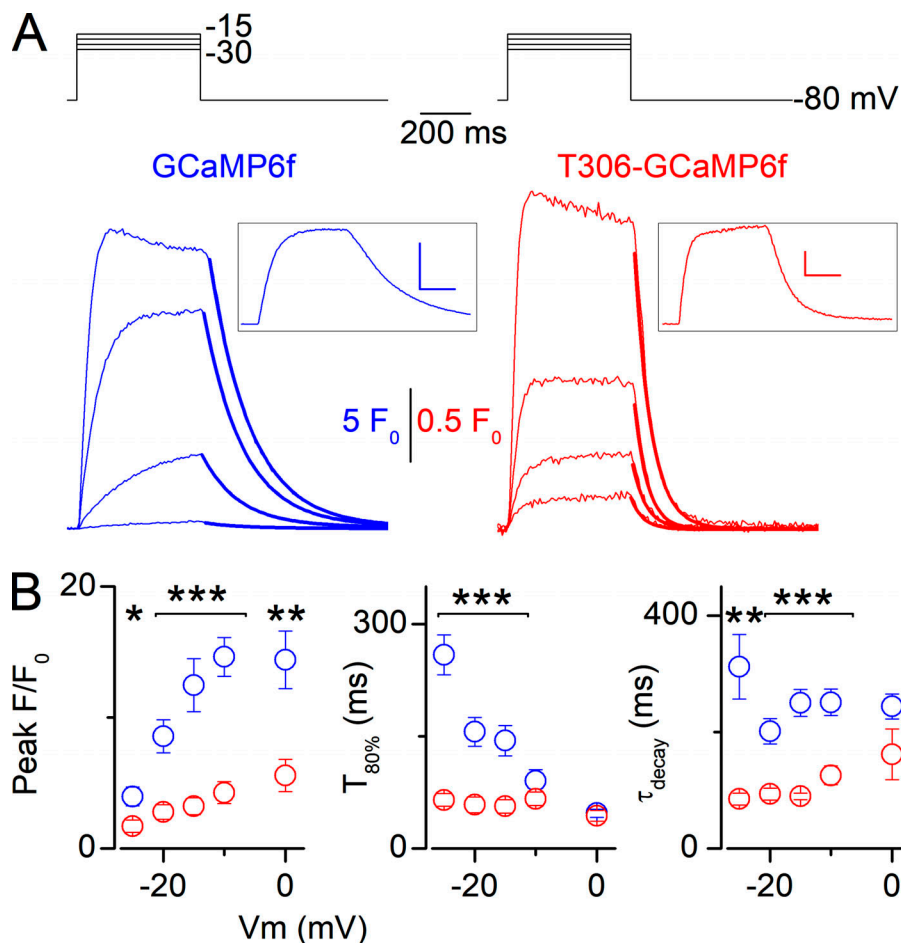
Figure 5. **Voltage-dependent GCaMP6f and T306-GCaMP6f Ca²⁺ transients. (A)** Illustrative examples of fluorescence transients from a muscle fiber expressing GCaMP6f (left) and a fiber expressing T306-GCaMP6f (right) in response to 500-ms-long depolarizing pulses of increasing amplitude. The curves superimposed to the decay of the transients correspond to the result from fitting a single exponential to the decay phase. The inset in each panel shows the average trace in response to a pulse to −15 mV from seven fibers expressing GCaMP6f (left) and six fibers expressing T306-GCaMP6f (right). **(B)** Mean voltage dependence of GCaMP6f (open blue circles) and T306-GCaMP6f (open red circles) fluorescence transients F/F_0 peak amplitude (Peak F/F_0), time to 80% peak amplitude ($T_{80\%}$), and time constant of decay (τ_{decay}). Mean values at the different voltage levels are from 7–14 fibers for GCaMP6f and 3–11 fibers for T306-GCaMP6f. Vertical bars represent the SEM. *, $P \leq 0.05$; **, $P \leq 0.01$; ***, $P \leq 0.001$.

reach 80% of the peak transient and the time constant of decay are reported in Fig. 8 D. The simulation predicted minimum differences in time course of rise and of decay of the transients between the two probes, consistent with the experimentally observed qualitative similar time courses of the transients from the two probes. However, the model did not reproduce the quantitative differences observed for the low levels of Ca²⁺ release activation (Fig. 5 B) for which the rate of rise and of decay of the T306-GCaMP6f transients were substantially elevated as compared with GCaMP6f. In an attempt to reproduce the experimentally observed differences, we tested a number of alternative combinations of parameters. One example is illustrated in Figs. S2, S3, and S4, which reproduce Figs. 6, 7, and 8, respectively, except that the value for the Ca²⁺ diffusion coefficient was reduced to 0.02 µm².ms⁻¹. Although this value seems unrealistic for the diffusion coefficient, in the current framework of the model, this represents the situation where the diffusion of calcium away from the release site is restricted. Under the simulated conditions, there would be basically no change in [Ca²⁺] at the center of the sarcomere. Even in such an extreme situation, the time course of GCaMP6f and T306-GCaMP6f would still not differ so markedly at the low levels of Ca²⁺ release activation (Fig. S4, C and D). One alternative possibility to explain differing kinetics between GCaMP6f and T306-GCaMP6f would be if GCaMP6f is in excess concentration as compared with the targeted version. A simulation of this situation is shown in Fig.

S5, assuming the concentration of GCaMP6f to be 10 times larger than that of T306-GCaMP6f. It shows that this condition better reproduces the experimentally observed differences in terms of time course of rise and of decay of the Ca²⁺-bound probe concentration. A more limited production of T306-GCaMP6f as compared with GCaMP6f and/or restricted T306-driven accumulation of GCaMP6f in the junctional SR membrane may thus occur and result in a lower amount of targeted probe molecules per volume unit.

Enhanced kinetic discrepancies between GCaMP6f and T306-GCaMP6f Ca²⁺ transients in the presence of EGTA

To characterize Ca²⁺ transients from GCaMP6f and T306-GCaMP6f throughout the entire range of muscle fiber voltage activation, we performed experiments in the presence of a high concentration of intracellular EGTA (see Solutions) to completely eliminate contraction. Corresponding GCaMP6f and T306-GCaMP6f transients triggered by depolarizing pulses to values ranging between −40 and +20 mV are shown in Fig. 9 A. Under these conditions too, the peak amplitude of T306-GCaMP6f transients was reduced (by two to three times) as compared with that of GCaMP6f transients (Fig. 9 B, left). In addition, the time course of rise (Fig. 9 B, right) and decay of the transients strongly differed, with T306-GCaMP6f transients exhibiting faster kinetics for all values of depolarization. Using model simulations, we tested a number of combinations of
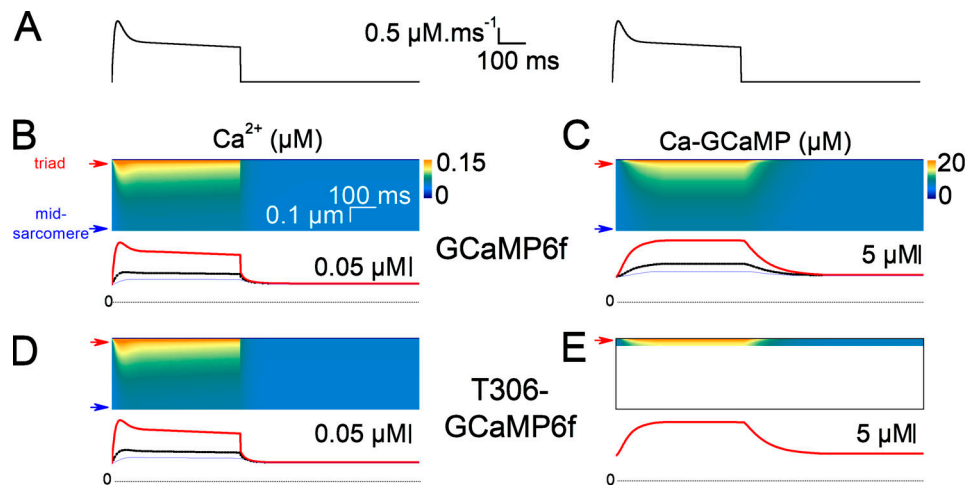
Figure 6. **Model simulation of the spatial gradient of Ca²⁺ and of calcium bound to the GCaMP6f probes along a 0.5-µm distance from the Ca²⁺ release site following a low level of SR Ca²⁺ release activation. (A)** Synthetic Ca²⁺ release input flux. **(B and C)** Spatial gradient of Ca²⁺ change (B) and corresponding Ca²⁺ bound to GCaMP6f (C). **(D and E)** Spatial gradient of Ca²⁺ change (D) and corresponding Ca²⁺ bound to T306-GCaMP6f (E). In B–E, traces underneath the image show the time course of change in the given parameter at the triad level (thick red trace), at the mid-sarcomere level (thin blue trace), and the average change throughout the distance (dotted black trace).

parameters to try to reproduce this discrepancy, but with no success. We suspect that protons liberated by EGTA upon Ca²⁺ binding affect both GCaMP6f and T306-GCaMP6f transients, but in a distinctive manner. Indeed, this is reminiscent of our previous work with a voltage-sensitive probe (Sanchez et al., 2018), which detected Ca²⁺ release–induced acidification when targeted to the junctional SR membrane, but not when present in the t-tubule membrane. A similar effect may be occurring here, with the targeted probe facing a stronger and

faster acidification than the nontargeted one. This may be the reason why T306-GCaMP6f transients routinely exhibited a negative component of fluorescence, as illustrated by the portion of trace indicated by an arrow in Fig. 9 A. The appearance of protons dissociating from the site to which calcium binds, on EGTA, was not dealt with in the simulation. Nevertheless, even if unresolved, this discrepancy at least is a straight indication that the two probes are facing a distinct environment.
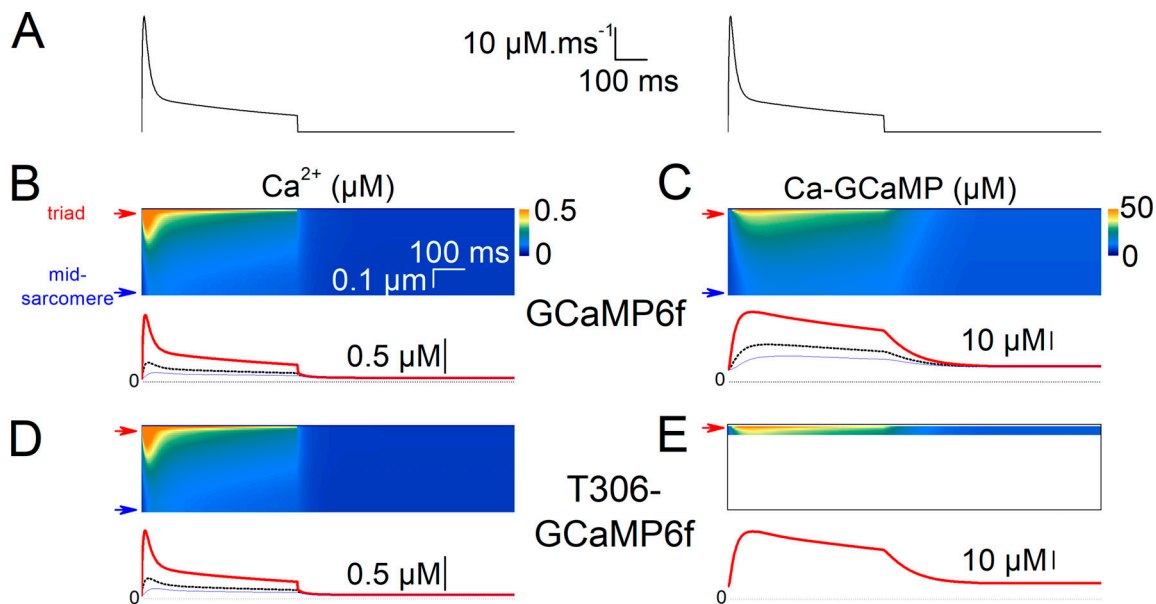

Figure 7. **Model simulation of the spatial gradient of Ca²⁺ and of calcium bound to the GCaMP6f probes along a 0.5-µm distance from the Ca²⁺ release site following a large level of SR Ca²⁺ release activation. (A)** Synthetic Ca²⁺ release input flux. **(B and C)** Spatial gradient of Ca²⁺ change (B) and corresponding Ca²⁺ bound to GCaMP6f (C). **(D and E)** Spatial gradient of Ca²⁺ change (D) and corresponding Ca²⁺ bound to T306-GCaMP6f (E). In B–E, traces underneath the image show the time course of change in the given parameter at the triad level (thick red trace), at the mid-sarcomere level (thin blue trace), and the average change throughout the entire distance (dotted black trace).
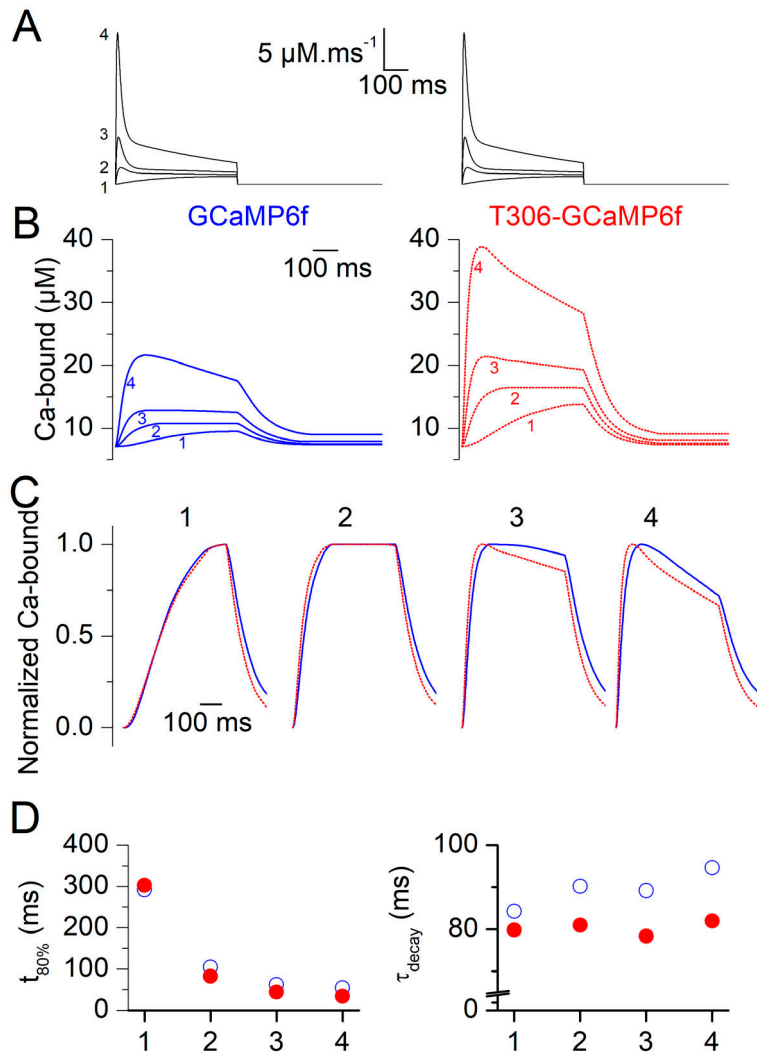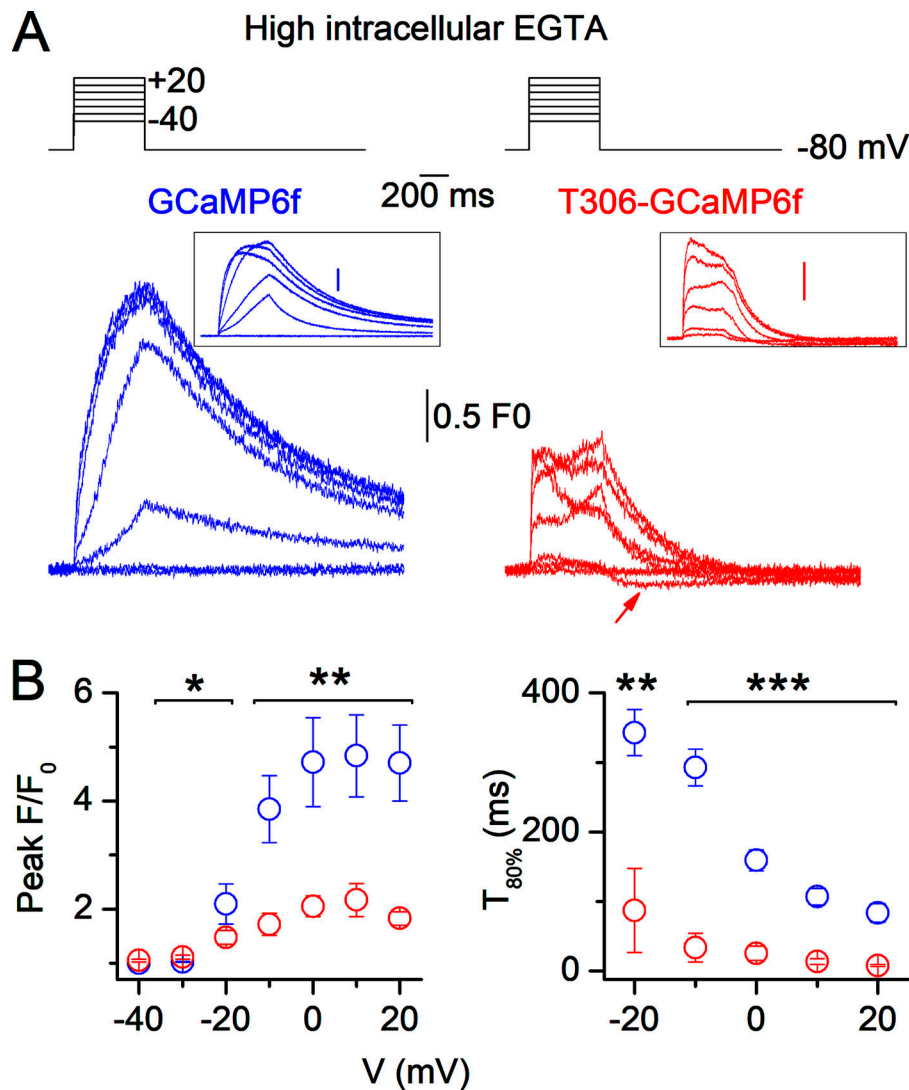
Figure 8. **Model simulation of the average changes in Ca²⁺ bound to GCaMP6f and to T306-GCaMP6f following different levels of SR Ca²⁺ release activation. (A)** Superimposed synthetic Ca²⁺ release input fluxes used for the simulation (1–4). **(B)** Calculated average changes in Ca²⁺ bound to GCaMP6f (left, blue) or T306-GCaMP6f (right, red) following each of the four Ca²⁺ release input fluxes shown in A. **(C)** Normalized time course of the calculated average changes in Ca²⁺ bound to GCaMP6f (continuous blue traces) and T306-GCaMP6f (dotted red traces) in response to the Ca²⁺ release fluxes shown in A. Changes in Ca²⁺ bound to each of the two probes for a same given input flux are shown superimposed. **(D)** Dependence upon the input flux (1–4) of the time to reach 80% of the peak change in Ca²⁺ bound to GCaMP6f (left, open blue circles) and T306-GCaMP6f (filled red circles) and corresponding values for the time constant of decay (right) after the end of the release flux.

Voltage-activated local changes in T306-GCaMP6f fluorescence

Despite reporting Ca²⁺ changes with corrupted kinetics and within a limited concentration range, one great advantage of T306-GCaMP6f over diffusible Ca²⁺ probes is its potential to track the occurrence and duration of triadic Ca²⁺ changes at various locations of a given muscle fiber and thus provide insights into the spatial variability of SR Ca²⁺ release upon activation of a muscle fiber. To this aim, we examined the changes in T306-GCaMP6f fluorescence at different positions along the scanned line. In these experiments, a slow scan frequency of 7.7 ms per line was used to improve the signal-to-noise ratio. Illustrative examples are presented in Fig. 10, which shows local changes from a muscle fiber stimulated by 0.5-s-long depolarizing pulses to –25 (Fig. 10 A), –20 (Fig. 10 B), and –15 mV (Fig. 10 C). In each panel, the top-left image corresponds to the raw line-scan fluorescence record, with the baseline fluorescence intensity profile along the line next to it on the left. The corresponding F/F₀ image is shown on the right; for this, F/F₀ was calculated for series of 5 pixels (0.1 µm per pixel) along the

line, each series centered on one peak of baseline fluorescence intensity. The five noisy traces underneath correspond to changes in F/F₀ at adjacent triadic locations within the region highlighted by a red box in the F/F₀ image. The smooth trace at the bottom represents the average change in F/F₀ throughout the entire line. Overall, Fig. 10 illustrates the fact that within a given image, there was remarkable consistency in terms of occurrence, time course and amplitude of the transients at the different locations, and this for all voltage levels. The series of traces in Fig. 10 A illustrates one rare example (fourth trace from top) of a particular location that could be identified where no response was detected, but otherwise, within the limits of the uncertainty due to the noise, local transients were very similar throughout. To quantitatively assess the spatial variability of the T306-GCaMP6f response, the onset time, peak amplitude, and full width at half-maximum (FWHM) of the signal were measured at eight random locations along lines scanned in six muscle fibers depolarized by pulses to values ranging between –25 and –10 mV. Fig. 11 reports the individual values for each parameter in the different fibers. Values for peak amplitude

Figure 9. **Voltage-dependent GCaMP6f and T306-GCaMP6f Ca²⁺ transients in the presence of intracellular EGTA. (A)** Illustrative examples of fluorescence transients from a muscle fiber expressing GCaMP6f (left) and a fiber expressing T306-GCaMP6f (right) in response to 500-ms-long depolarizing pulses of increasing amplitude. The inset in each panel shows the average traces in response to the same protocol from six fibers expressing GCaMP6f (left, blue) and from four fibers expressing T306-GCaMP6f (right, red). **(B)** Mean voltage dependence of GCaMP6f (blue circles) and T306-GCaMP6f (red circles) F/F_0 peak amplitude (peak F/F_0) and time to 80% peak amplitude ($T_{80\%}$) from muscle fibers expressing GCaMP6f and T306-GCaMP6f, respectively. Mean values at the different voltage levels are from 5–9 fibers for GCaMP6f and 4–12 fibers for T306-GCaMP6f. Vertical bars represent the SEM. *, $P \leq 0.05$; **, $P \leq 0.01$; ***, $P \leq 0.001$.

(peak F/F_0), FWHM, and onset time (T_O, relative to time of pulse initiation) for each of the eight T306-GCaMP6f local fluorescence transients are reported in Fig. 11 B in the different fibers (symbol coded). Traces on the top show examples of most differing fluorescence transients among the eight tested triadic regions of lines scanned in the filled-square–coded fiber. Overall, results show that within the limits imposed by the sampling rate and signal-to-noise level, there was limited detectable variability in the onset time and FWHM of the transients detected in response to a given voltage pulse at distinct triadic locations of a given muscle fiber. On the other hand, for a given depolarizing level, the peak amplitude could substantially differ between distinct locations of a given fiber, for instance by a factor up to 2 for the largest depolarizing pulse in Fig. 11 B. This may be evidence for spatial disparity in the activation level of RYR1 channels at distinct triadic regions of a same fiber.

Targeting GCaMP6f to the t-tubule side of the triadic junction
Given its ~10-times-smaller size than one RYR1 monomer, GCaMP6f when fused to the T306 domain is likely to sit close to the foot region of the channel, underneath or near the lateral side of the massive cytosolic domain. We questioned whether targeting GCaMP6f to an alternative triadic location, specifically the t-tubule side, may provide distinct results. This was also expected to provide information as to whether the specific fusion of GCaMP6f to T306 could be responsible for some of the differences observed with GCaMP6f Ca²⁺ transients. To this aim, we fused the Ca$_V$1.1 auxiliary subunit γ1 to GCaMP6f, anticipating that it would convey the probe to face the exterior side of the RYR1 cytosolic domain. As the N-terminal half of the γ1-subunit is thought to be required for association with the full dihydropyridine receptor complex through its association with the Ca$_V$1.1 subunit (Arikkath et al., 2003), GCaMP6f was fused to its C-terminal end after the insertion of a 29-amino-acid-long rigid H4-type linker (Amet et al., 2009; see Materials and methods). In contrast to T306-GCaMP6f, the expression of γ1-GCaMP6f was not restricted to a local area around one nucleus (or to a few of such areas each surrounding a nucleus) but occupied vast fiber regions, if not the entire fiber. The expression pattern of γ1-GCaMP6f fluorescence was typically triadic (Fig. 12 A), consistent with localization in the t-tubule membrane. As observed with T306-GCaMP6f, voltage-activated γ1-GCaMP6f
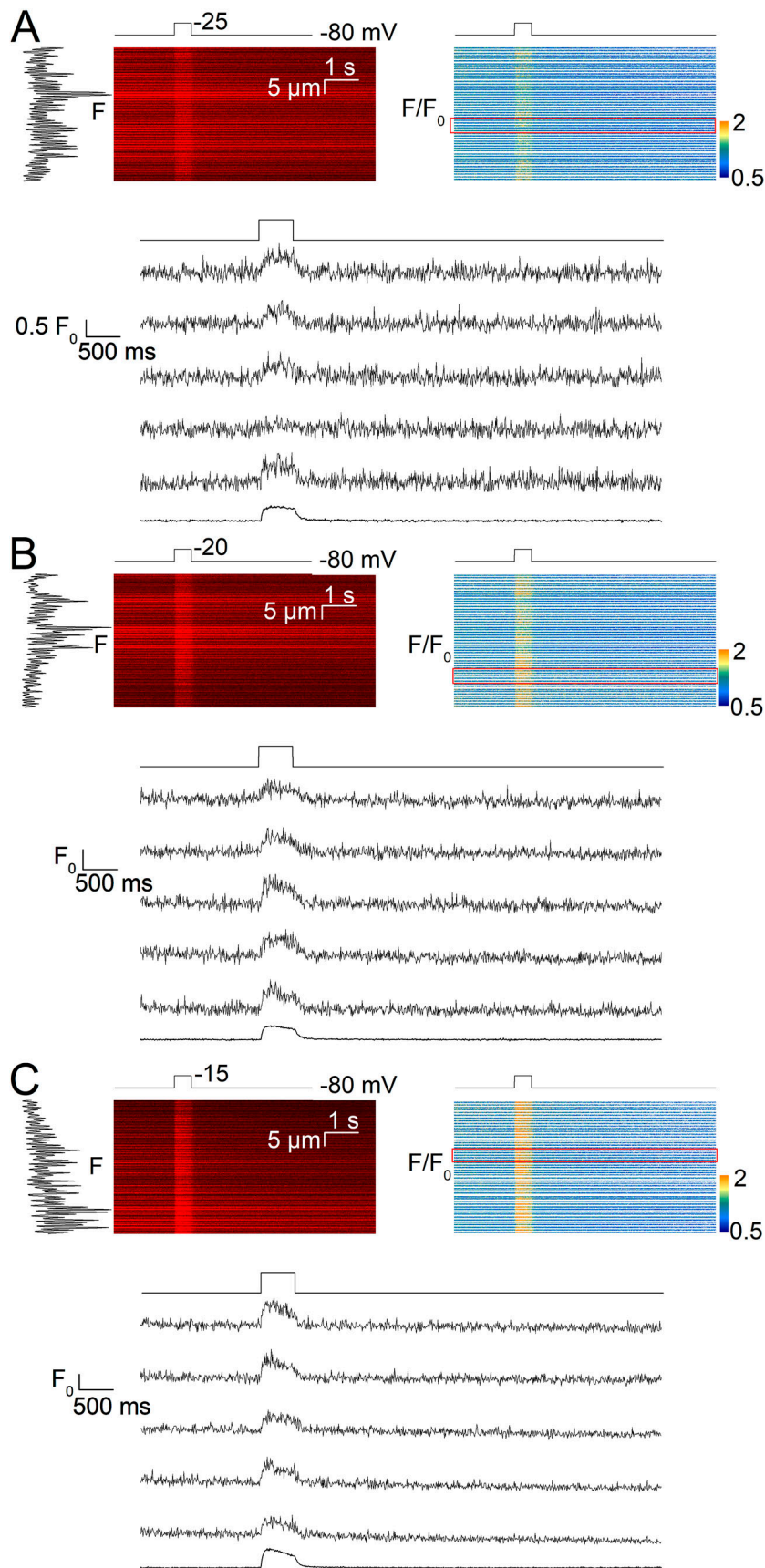
Figure 10. **Local changes in T306-GCaMP6f fluorescence in response to different levels of SR Ca²⁺ release activation. (A–C)** Line-scan images (7.7 ms per line) of T306-GCaMP6f fluorescence are from the same muscle fiber depolarized for 500 ms to −25 (A), −20 (B), and −15 mV (C). In each panel, the raw line-scan fluorescence record is shown on the left with the F_0 intensity profile along the line next to it. The corresponding F/F_0 image is shown on the right; values were calculated for series of five adjacent pixels centered on each of the successive peaks of F_0 fluorescence along the line. The five traces at the bottom correspond to changes in F/F_0 at adjacent locations within the red box region superimposed to the F/F_0 image. The smooth trace at the bottom corresponds to the average change in F/F_0 throughout the entire line.
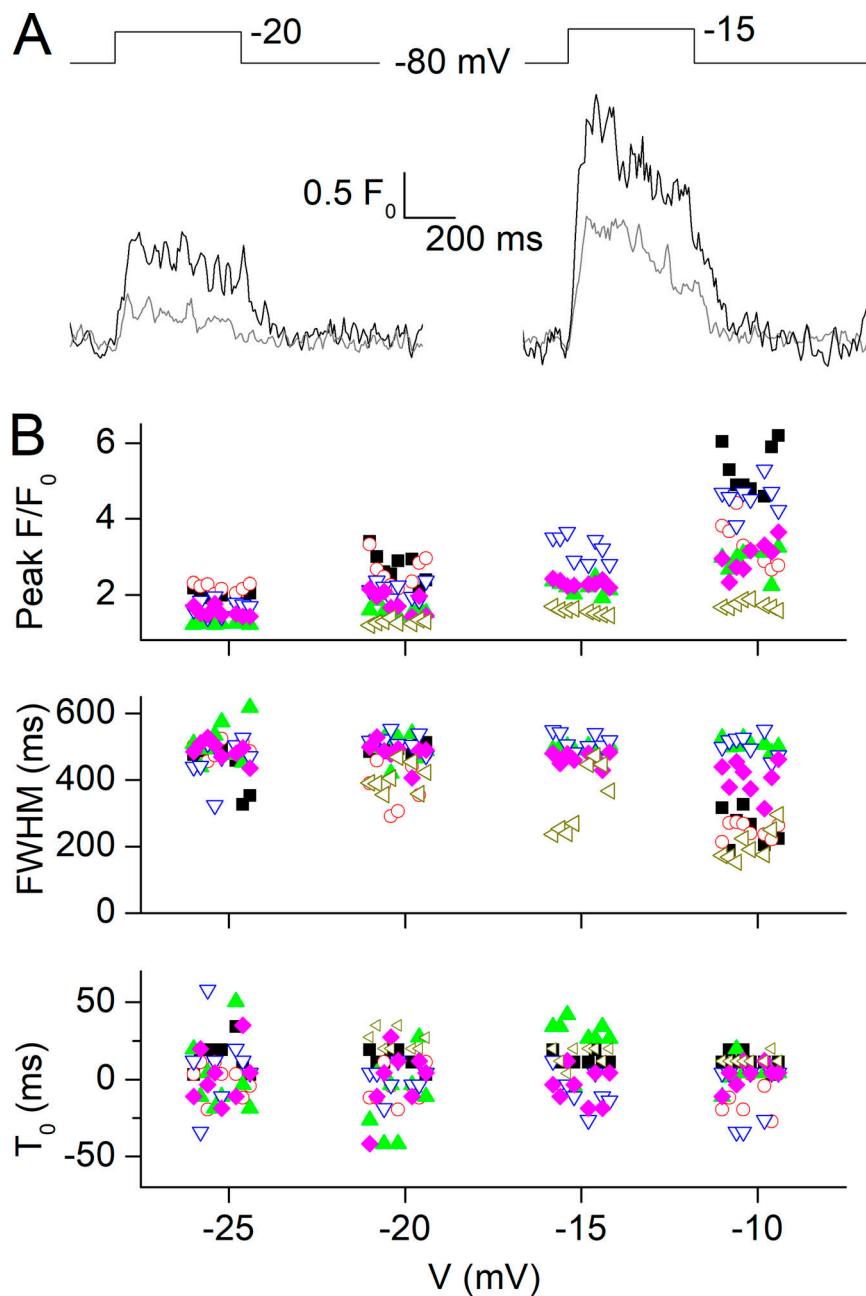
Figure 11. Properties of the local changes in T306-GCaMP6f fluorescence upon SR Ca²⁺ release activation. (A) Illustrative examples of two most differing T306-GCaMP6f fluorescence transients at distinct triadic locations of a given muscle fiber depolarized to −20 and −15 mV. **(B)** Individual values for peak F/F_0, FWMH and onset time (T_0, relative to time of pulse initiation) from local T306-GCaMP6f fluorescence transients collected as shown in Fig. 9 at eight random locations along lines scanned in six muscle fibers depolarized to −25, −20, −15, and −10 mV. Each symbol corresponds to a different fiber. T_0 was determined by fitting a linear function to the early rising phase of the F/F_0 transients. From extrapolating the fit earlier in time, the x axis value of the data point that was the closest in time to the intersection of the fit with the F/F_0 value of 1 was assumed to be T_0. Because of the noise in the transients and the slow sampling rate, this procedure sometimes generated values earlier than the onset of the pulse.

transients were smaller in amplitude than GCaMP6f transients (Fig. 12, B and C, left panel) and also yielded a faster time course of decay (Fig. 12 C, right panel). However, different from T306-GCaMP6f, the time course of rise of γ1-GCaMP6f transients appeared not to quantitatively differ from that of GCaMP6f, thus more consistent with the results from the simulation whatever the Ca²⁺ release activation level (Fig. 8, C and D). Voltage-activated γ1-GCaMP6f fluorescence transients at different spatial locations of a scanned line were also compared. Fig. 13 shows such local changes from a muscle fiber stimulated by 0.5-s-long depolarizing pulses to −25 (Fig. 13 A), −20 (Fig. 13 B), and −15 mV (Fig. 13 C). The image in each panel shows the time-dependent (horizontal axis) F/F_0 signal at successive triadic locations (vertical axis) along a scanned line. For this, adjacent series of five contiguous lines in the original γ1-GCaMP6f line-scan image

(corresponding to five adjacent pixel positions, 0.1 µm per pixel) were averaged, each series being centered on the position of a peak of baseline fluorescence intensity (as described in relation to Fig. 10). The five noisy traces underneath each F/F_0 image correspond to adjacent transients within the region highlighted by a red box in the F/F_0 image. The smooth trace at the bottom represents the average change in F/F_0 throughout the entire line. As observed with T306-GCaMP6f, fluorescence transients at distinct triadic locations were similar in terms of amplitude, time of onset, time of termination, and general time course. However, it is noticeable that these triadic γ1-GCaMP6f transients occasionally exhibited temporally distinct abrupt subchanges which we think could witness discrete sub-levels of Ca²⁺ release due to transient activation or closure of a coherent group of RYR1 channels. More explicit illustrations of such
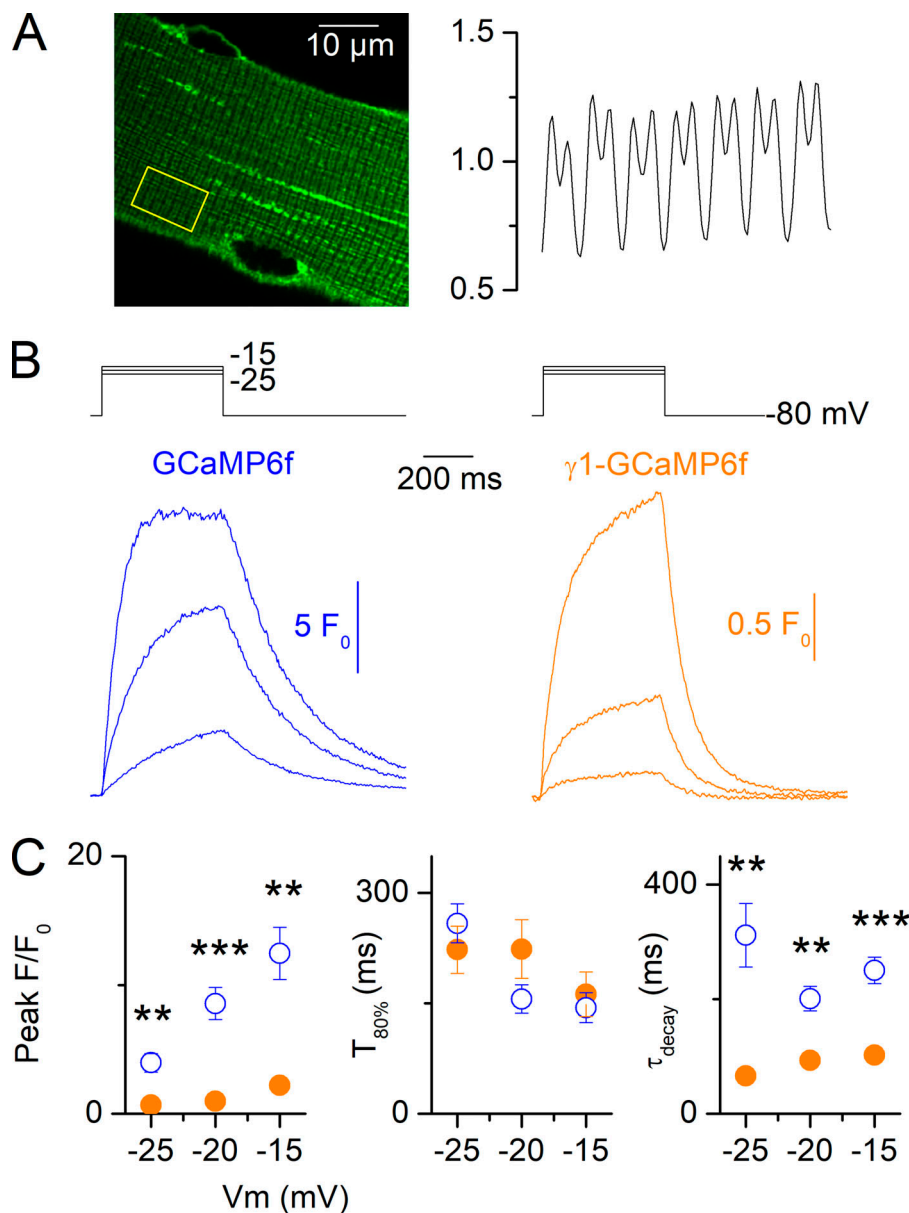
Figure 12. **Voltage-dependent GCaMP6f and γ1-GCaMP6f Ca²⁺ transients. (A)** Subcellular fluorescence pattern of γ1-GCaMP6f. The graph on the right shows the fluorescence profile along the highlighted box region in the x,y image. **(B)** Illustrative examples of fluorescence transients from a muscle fiber expressing GCaMP6f (left, blue) and from a fiber expressing γ1-GCaMP6f (right, orange) in response to 500-ms-long depolarizing pulses to −25, −20, and −15 mV. **(C)** Mean voltage dependence of GCaMP6f (open circles) and γ1-GCaMP6f (filled circles) fluorescence transients F/F_0 peak amplitude (Peak F/F_0), time to 80% peak amplitude ($T_{80\%}$) and time constant of decay (τ_{decay}). Mean values at the three voltage levels are from 7–14 fibers for GCaMP6f and 5–7 fibers for γ1-GCaMP6f. Vertical bars represent the SEM. **, $P \leq 0.01$; ***, $P \leq 0.001$.

events are presented in Fig. 14, which shows two γ1-GCaMP6f F/F_0 images from a fiber challenged by a 2-s-long pulse to −25 mV (left) and −20 mV (right). Images were processed as in Fig. 13. The five traces at the bottom of each image correspond to the fluorescence signal at the positions indicated by black arrows in the above-corresponding F/F_0 image. Examples of distinct fluorescence subchanges are highlighted by red arrows.

Discussion

Progress in understanding RYR1 physiological function and regulation in normal and diseased skeletal muscle requires improving our capabilities to detect RYR1 channel activity in intact differentiated muscle fibers, ultimately down to the single-channel level. The present work is the first attempt to detect Ca²⁺ signals with genetically encoded probes targeted to the triadic region of differentiated skeletal muscle fibers.

Primary evidence that we succeeded in targeting T306-GCaMP6f specifically to the junction is the typical spatial pattern of fluorescence, similar to the previously observed one when expressing in the same preparation either RYR1 channels (Lefebvre et al., 2011) or T306-fused with biosensors of the Mermaid family from which functional assays proved that the T306 domain did convey the biosensors to the triadic SR membrane (Sanchez et al., 2018). Of interest, we expect T306-GCaMP6f to be in close vicinity to the RYR1 channels, because the T306 sequence contains the KEKE domain believed to be essential for triadin binding to RYR1 and calsequestrin (Kobayashi et al., 2000; Lee et al., 2004). The transversal banded pattern of γ1-GCaMP6f fluorescence is also consistent with triadic localization, and since γ1 is an accessory partner of $Ca_V1.1$, there is little doubt that this construct was present in the t-tubule membrane.
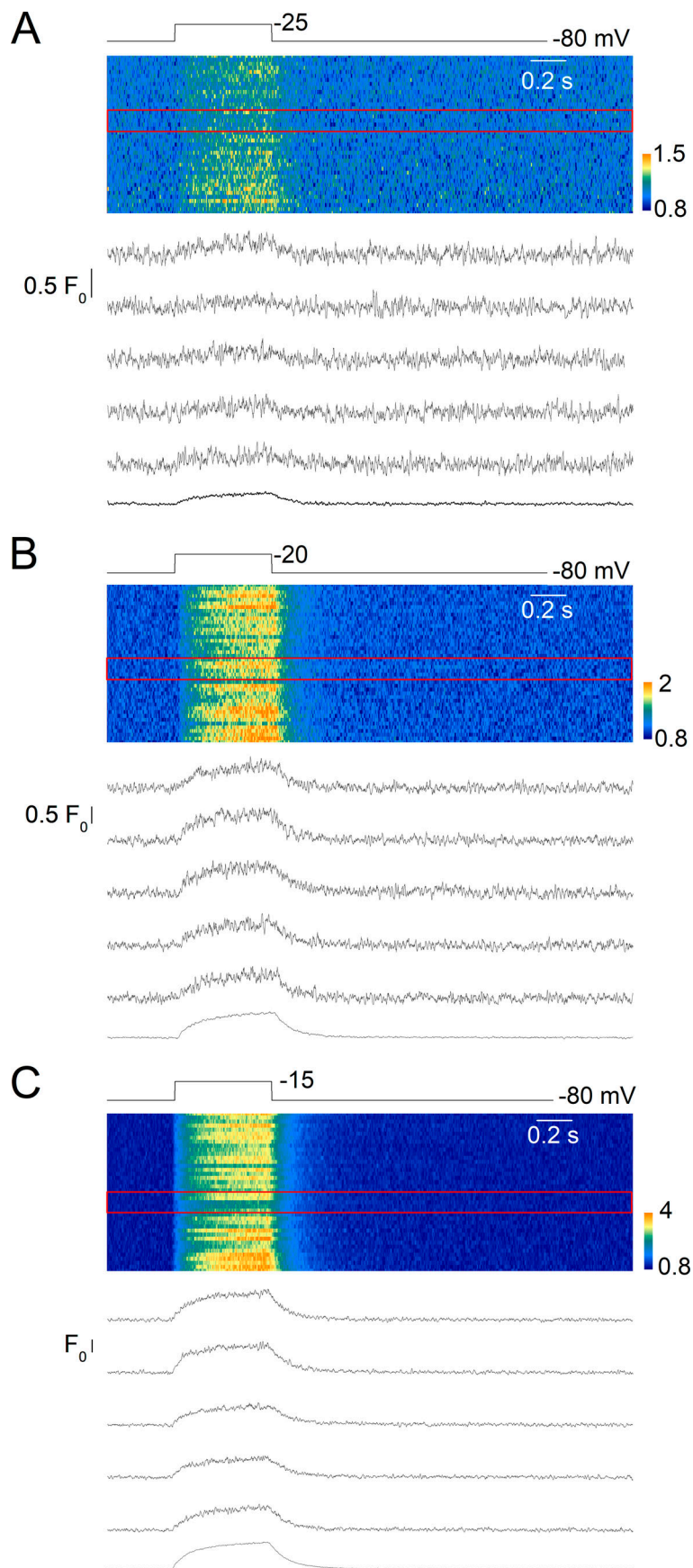
Figure 13. **Local changes in γ1-GCaMP6f fluorescence in response to different levels of SR Ca²⁺ release activation. (A–C)** Line-scan images (4.95 ms per line) of γ1-GCaMP6f fluorescence were recorded from a same muscle fiber depolarized for 500 ms to −25 (A), −20 (B), and −15 mV (C). In each panel, the color-coded image on top corresponds to the F/F_0 fluorescence transients detected at triadic locations of the initial line-scan image. Each pixel line in the image corresponds to the F/F_0 signal averaged over a series of five pixels (0.1 µm per pixel) centered on one peak of baseline fluorescence intensity. The five noisy traces underneath each F/F_0 image correspond to adjacent transients within the region highlighted by a red box. The bottom smooth trace corresponds to the average change in F/F_0 throughout the entire line.

Sanchez et al.
Triadic Ca²⁺ changes in skeletal muscle

Journal of General Physiology   16 of 20
https://doi.org/10.1085/jgp.202012592
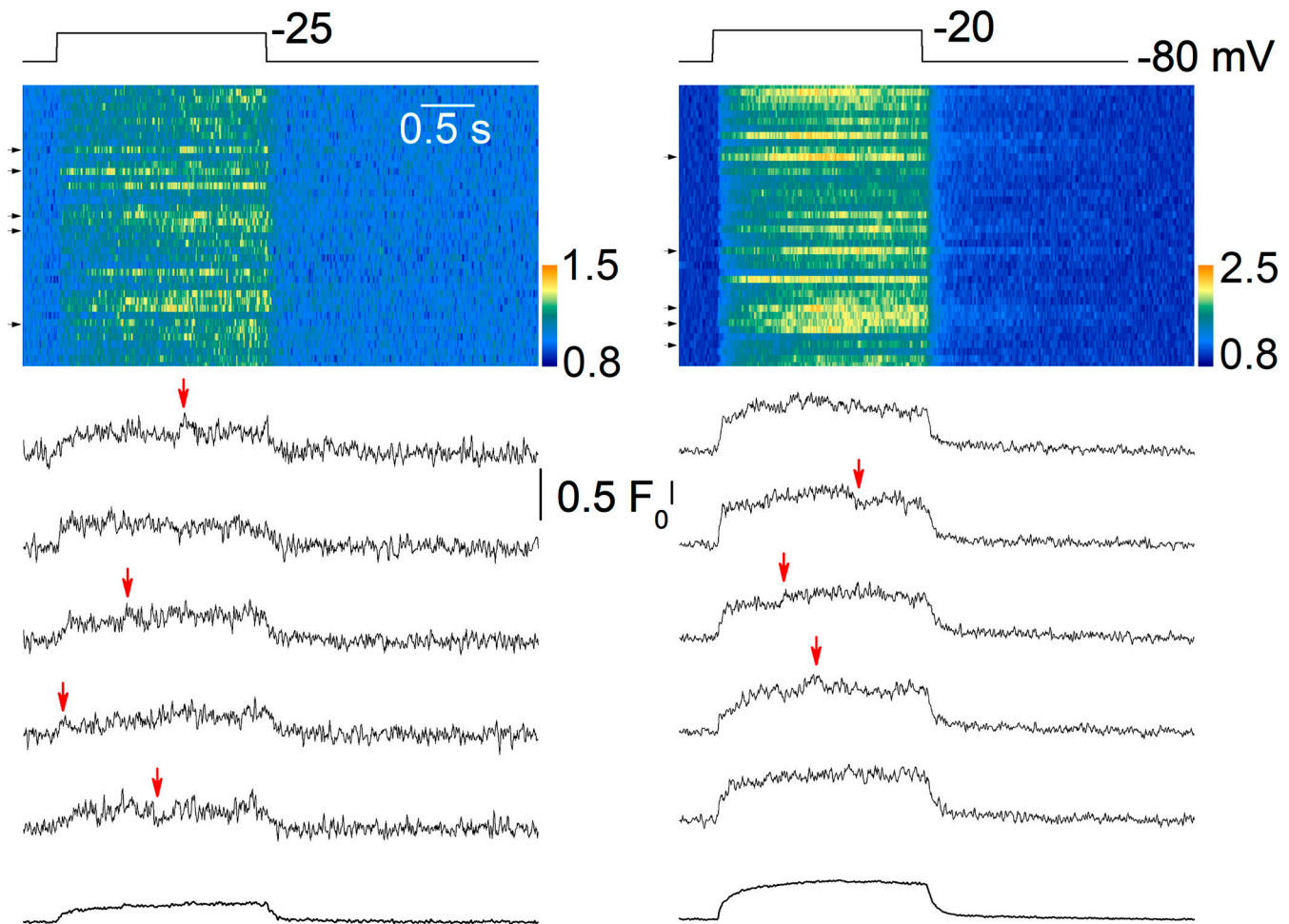
Figure 14. **Local changes in γ1-GCaMP6f fluorescence in response to 2-s-long depolarizing pulses.** Line-scan images (4.95 ms per line) of γ1-GCaMP6f fluorescence were recorded from a muscle fiber while a 2-s-long depolarizing pulse from −80 mV to −25 (left) and then from −80 mV to −20 mV (right) were applied. Each panel is constructed as described in Fig. 13, except that the individual F/F₀ traces shown were selected at the positions indicated by arrows next to the color-coded line-scan image (from top to bottom, respectively). Arrows point to a few examples of time points when subchanges in fluorescence could be observed during the voltage-induced transients.

Two aspects related to targeting of the probes need to be considered. The first is the possibility that T306 and/or γ1 and/or the specific composition of the triadic nanoenvironment alter the intrinsic properties of the Ca²⁺-sensing probe. Results from our calibration suggest that the affinity for Ca²⁺ does not substantially differ between GCaMP6f and T306-GCaMP6f, and we assume this is also the case for γ1-GCaMP6f given the similarity of the corresponding voltage-activated fluorescence transients. Interestingly, the peak amplitude of the transients from the two targeted probes appears to substantially differ from the untargeted one, with GCaMP6f generating peak F/F₀ values routinely approximately three to four and six to eight times greater than T306-GCaMP6f and γ1-GCaMP6f, respectively, under the same conditions of stimulation. One would have expected the opposite. Indeed, it is difficult to foresee that Ca²⁺ changes in the triadic cleft are smaller than in the bulk. One possible explanation would be if resting triadic Ca²⁺ concentration is maintained at an elevated level as compared with the bulk, so that targeted probe molecules would be heavily Ca²⁺ saturated at rest. A simulation assuming a resting triadic Ca²⁺ concentration

level of 0.5 μM showed that this situation would result in a reduced amplitude of the T306-GCaMP6f F/F₀ transients as compared with transients from the nontargeted probe. Although consistent with the experimental data, we prefer to remain careful with this possibility, as there is, to our knowledge, neither experimental evidence nor conceptual framework that would endorse a triadic Ca²⁺ level constantly maintained at a 10 times higher level than the bulk. Alternative possibilities may be considered that would contribute explaining the experimentally observed reduced amplitude of the F/F₀ signal from the targeted probe. Following suggestions from the editor and one of the reviewers of this manuscript, the targeted probe may not be as constrained as assumed, and the nontargeted probe heterogeneous distribution (see Fig. 1 B) and/or heterogeneous reactivity may need to be considered. The blurring of the microscope might also affect the observations and introduce a spatial averaging effect, impacting differently observations made with the targeted and the nontargeted probe. Although we cannot rule out that other triadic-restricted alterations in cytosolic environment may play a role in this difference, it could also well be

that both the C-terminal and N-terminal fusion of GCaMP6f to T306 and γ1, respectively, alters its quantum yield, in agreement with the difference between our estimates of F_{max}/F_{min} for T306-GCaMP6f as compared with commonly reported values for GCaMP6f.

The other issue to be considered is whether localization of the probe at the triad may affect EC coupling. The results establish that they did not completely compromise activation of RYR1 channels. The patchy localization of T306-GCaMP6f allowed us to test whether Ca^{2+} transients differ between two regions of a same fiber exhibiting a different level of probe expression. The results provided no reproducible indication that this is the case. However, they do not rule out the possibility, as even a very low expression level of T306-GCaMP6f could be speculated to affect SR Ca^{2+} release. In the case of γ1, previous investigations on muscle fibers from γ1-deficient mice showed that this $Ca_V1.1$ partner promotes voltage-dependent inactivation of Ca^{2+} release (Andronache et al., 2007). However, this does not imply that overexpression of γ1 further enhances this effect as compared with the normal situation, and it is not clear if there is any overexpression in our experimental conditions (for instance, see Fig. 10 in Lefebvre et al., 2011, showing no RYR1 overexpression in fibers expressing EGFP-RYR1 under the same conditions of transfection).

Fluorescence transients from untargeted and triad-targeted GCaMP6f are slower than rhod-2 transients, in agreement with the known kinetic limitations of the probes. Conversely, and somewhat unexpectedly, the time courses of untargeted and triad-targeted GCaMP6f transients do not strongly differ from each other, even though the triadic probes have to experience larger changes in Ca^{2+} than the bulk. Intuition is unreliable, because model simulations proved that kinetic delays of the probe's response, together with the fact that GCaMP6f detects the average Ca^{2+} throughout the sarcomere, contribute to dampen detection of differences in the actual time course of Ca^{2+} changes at and away from the triad with this approach. In the future, one possibility to assess this gradient would be to compare the T306-GCaMP6f response with that of GCaMP6f targeted to the mid-sarcomere region. For now, we have found that the overall qualitatively similar experimental observations with triad-targeted and nontargeted GCaMP6f are consistent with model predictions based on quantitative knowledge of the main processes involved in the control of intracellular Ca^{2+}, assuming the targeted and nontargeted probes exhibit the same affinity and kinetic properties. Still, certain quantitative discrepancies between the time course of experimentally detected untargeted and targeted GCaMP6f fluorescence transients could not be reproduced by our standard simulations. For instance, a minimal difference in the rate of rise of the transients was predicted, as approximated by the time to reach 80% of the peak fluorescence. Nevertheless, for low-intermediate levels of Ca^{2+} release activation, this parameter appeared to be very substantially reduced for T306-GCaMP6f transients as compared with both GCaMP6f and γ1-GCaMP6f transients. Also, following the end of pulses up to −10 mV, fluorescence transients from triad-targeted probes decayed approximately twice faster than transients from untargeted GCaMP6f, whereas the simulated difference was much

less. Further adjustments of the model parameters may be able to reproduce these differences. For instance, our standard modeling assumed that targeted and untargeted probes were present at an identical concentration; this may not be the case and could contribute to the experimentally reported kinetic differences (e.g., Fig. S5).

One major interest of targeting the probes is the possibility to simultaneously assess the behavior of distinct Ca^{2+} release regions within a same muscle fiber. We found that such local voltage-activated T306-GCaMP6f fluorescence transients exhibit remarkably constant features in terms of time of onset and of termination at a given level of activation. An alternative way to look at it is to highlight what was not detected. Concerning this matter, we initially thought that at low levels of SR Ca^{2+} release activation, we would be able to identify such phenomena as a mix of activated and nonactivated triadic regions in a same image or Ca^{2+} transients starting after a delay following the beginning of the pulse, but we either did not or did extremely rarely (e.g., Fig. 10 A). One ultimate objective of the present approach is detection of the activity of a single RYR1 channel or of a single group of channels. The limitations of the presently used probes in terms of affinity for Ca^{2+}, kinetics of response, and fluorescence yield still preclude such reliable detection. However, we provide preliminary evidence that temporally separated events and/or sublevels during the voltage-activated fluorescence transients could witness activation or closure of coherent clusters of RYR1 channels contributing to Ca^{2+} release.

In conclusion, although the high Ca^{2+} affinity and kinetic delays of GCaMP6f limit its use as a faithful triadic Ca^{2+} reporter, the targeted sensor provides unique access to the gross activity of a population of individual triads inside a muscle fiber. This may prove useful to characterize specific disease conditions associated with erratic behavior of RYR1 channels. This would be the case, for instance, of myotubular myopathy, for which there is an indication for spatially localized failure of SR Ca^{2+} release (Kutchukian et al., 2016), or of several situations presumably associated with a leaky behavior of the channels, for which there is no information so far as to how it operates in terms of RYR1 channel or RYR1 channel cluster activity (e.g., Lyfenko et al., 2007; Bellinger et al., 2009).

Acknowledgments

References

Amet, N., H.F. Lee, and W.C. Shen. 2009. Insertion of the designed helical linker led to increased expression of tf-based fusion proteins. *Pharm. Res.* 26:523–528. https://doi.org/10.1007/s11095-008-9767-0

Andronache, Z., D. Ursu, S. Lehnert, M. Freichel, V. Flockerzi, and W. Melzer. 2007. The auxiliary subunit gamma 1 of the skeletal muscle L-type Ca²⁺ channel is an endogenous Ca²⁺ antagonist. *Proc. Natl. Acad. Sci. USA.* 104:17885–17890. https://doi.org/10.1073/pnas.0704340104

Arikkath, J., C.C. Chen, C. Ahern, V. Allamand, J.D. Flanagan, R. Coronado, R.G. Gregg, and K.P. Campbell. 2003. Gamma 1 subunit interactions within the skeletal muscle L-type voltage-gated calcium channels. *J. Biol. Chem.* 278:1212–1219. https://doi.org/10.1074/jbc.M208689200

Barone, V., D. Randazzo, V. Del Re, V. Sorrentino, and D. Rossi. 2015. Organization of junctional sarcoplasmic reticulum proteins in skeletal muscle fibers. *J. Muscle Res. Cell Motil.* 36:501–515. https://doi.org/10.1007/s10974-015-9421-5

Baylor, S.M., and S. Hollingworth. 2003. Sarcoplasmic reticulum calcium release compared in slow-twitch and fast-twitch fibres of mouse muscle. *J. Physiol.* 551:125–138. https://doi.org/10.1113/jphysiol.2003.041608

Baylor, S.M., W.K. Chandler, and M.W. Marshall. 1982. Use of metallochromic dyes to measure changes in myoplasmic calcium during activity in frog skeletal muscle fibres. *J. Physiol.* 331:139–177. https://doi.org/10.1113/jphysiol.1982.sp014368

Bellinger, A.M., S. Reiken, C. Carlson, M. Mongillo, X. Liu, L. Rothman, S. Matecki, A. Lacampagne, and A.R. Marks. 2009. Hypernitrosylated ryanodine receptor calcium release channels are leaky in dystrophic muscle. *Nat. Med.* 15:325–330. https://doi.org/10.1038/nm.1916

Braubach, P., M. Orynbayev, Z. Andronache, T. Hering, G.B. Landwehrmeyer, K.S. Lindenberg, and W. Melzer. 2014. Altered Ca(2+) signaling in skeletal muscle fibers of the R6/2 mouse, a model of Huntington's disease. *J. Gen. Physiol.* 144:393–413. https://doi.org/10.1085/jgp.201411255

Brum, G., E. Ríos, and E. Stéfani. 1988. Effects of extracellular calcium on calcium movements of excitation-contraction coupling in frog skeletal muscle fibres. *J. Physiol.* 398:441–473. https://doi.org/10.1113/jphysiol.1988.sp017052

Chen, T.W., T.J. Wardill, Y. Sun, S.R. Pulver, S.L. Renninger, A. Baohan, E.R. Schreiter, R.A. Kerr, M.B. Orger, V. Jayaraman, et al. 2013. Ultrasensitive fluorescent proteins for imaging neuronal activity. *Nature.* 499:295–300. https://doi.org/10.1038/nature12354

Cheung, A., J.A. Dantzig, S. Hollingworth, S.M. Baylor, Y.E. Goldman, T.J. Mitchison, and A.F. Straight. 2002. A small-molecule inhibitor of skeletal muscle myosin II. *Nat. Cell Biol.* 4:83–88. https://doi.org/10.1038/ncb734

Csernoch, L., J. Zhou, M.D. Stern, G. Brum, and E. Ríos. 2004. The elementary events of Ca²⁺ release elicited by membrane depolarization in mammalian muscle. *J. Physiol.* 557:43–58. https://doi.org/10.1113/jphysiol.2003.059154

Csernoch, L., S. Pouvreau, M. Ronjat, and V. Jacquemond. 2008. Voltage-activated elementary calcium release events in isolated mouse skeletal muscle fibers. *J. Membr. Biol.* 226:43–55. https://doi.org/10.1007/s00232-008-9138-0

Despa, S., B. Shui, J. Bossuyt, D. Lang, M.I. Kotlikoff, and D.M. Bers. 2014. Junctional cleft [Ca²⁺]i measurements using novel cleft-targeted Ca²⁺ sensors. *Circ. Res.* 115:339–347. https://doi.org/10.1161/CIRCRESAHA.115.303582

Donahue, B.S., and R.F. Abercrombie. 1987. Free diffusion coefficient of ionic calcium in cytoplasm. *Cell Calcium.* 8:437–448. https://doi.org/10.1016/0143-4160(87)90027-3

Feldmeyer, D., W. Melzer, and B. Pohl. 1990. Effects of gallopamil on calcium release and intramembrane charge movements in frog skeletal muscle fibres. *J. Physiol.* 421:343–362. https://doi.org/10.1113/jphysiol.1990.sp017948

Flucher, B.E., A. Conti, H. Takeshima, and V. Sorrentino. 1999. Type 3 and type 1 ryanodine receptors are localized in triads of the same mammalian skeletal muscle fibers. *J. Cell Biol.* 146:621–630. https://doi.org/10.1083/jcb.146.3.621

Garcia, J., and M.F. Schneider. 1993. Calcium transients and calcium release in rat fast-twitch skeletal muscle fibres. *J. Physiol.* 463:709–728. https://doi.org/10.1113/jphysiol.1993.sp019618

Helassa, N., X.H. Zhang, I. Conte, J. Scaringi, E. Esposito, J. Bradley, T. Carter, D. Ogden, M. Morad, and K. Török. 2015. Fast-Response Calmodulin-Based Fluorescent Indicators Reveal Rapid Intracellular Calcium Dynamics. *Sci. Rep.* 5:15978. https://doi.org/10.1038/srep15978

Hernández-Ochoa, E.O., R.O. Olojo, R.T. Rebbeck, A.F. Dulhunty, and M.F. Schneider. 2014. β1a490-508, a 19-residue peptide from C-terminal tail of Cav1.1 β1a subunit, potentiates voltage-dependent calcium release in adult skeletal muscle fibers. *Biophys. J.* 106:535–547. https://doi.org/10.1016/j.bpj.2013.11.4503

Hollingworth, S., and S.M. Baylor. 2013. Comparison of myoplasmic calcium movements during excitation-contraction coupling in frog twitch and mouse fast-twitch muscle fibers. *J. Gen. Physiol.* 141:567–583. https://doi.org/10.1085/jgp.201310961

Jacquemond, V. 1997. Indo-1 fluorescence signals elicited by membrane depolarization in enzymatically isolated mouse skeletal muscle fibers. *Biophys. J.* 73:920–928. https://doi.org/10.1016/S0006-3495(97)78124-4

Klein, M.G., H. Cheng, L.F. Santana, Y.H. Jiang, W.J. Lederer, and M.F. Schneider. 1996. Two mechanisms of quantized calcium release in skeletal muscle. *Nature.* 379:455–458. https://doi.org/10.1038/379455a0

Kobayashi, Y.M., B.A. Alseikhan, and L.R. Jones. 2000. Localization and characterization of the calsequestrin-binding domain of triadin 1. Evidence for a charged beta-strand in mediating the protein-protein interaction. *J. Biol. Chem.* 275:17639–17646. https://doi.org/10.1074/jbc.M002091200

Kovacs, L., E. Rios, and M.F. Schneider. 1983. Measurement and modification of free calcium transients in frog skeletal muscle fibres by a metallochromic indicator dye. *J. Physiol.* 343:161–196. https://doi.org/10.1113/jphysiol.1983.sp014887

Kutchukian, C., M. Lo Scrudato, Y. Tourneur, K. Poulard, A. Vignaud, C. Berthier, B. Allard, M.W. Lawlor, A. Buj-Bello, and V. Jacquemond. 2016. Phosphatidylinositol 3-kinase inhibition restores Ca²⁺ release defects and prolongs survival in myotubularin-deficient mice. *Proc Natl Acad Sci USA* 113:14432–14437. https://doi.org/10.1073/pnas.1604099113

Lai, F.A., Q.Y. Liu, L. Xu, A. el-Hashem, N.R. Kramarcy, R. Sealock, and G. Meissner. 1992. Amphibian ryanodine receptor isoforms are related to those of mammalian skeletal or cardiac muscle. *Am. J. Physiol.* 263:C365–C372. https://doi.org/10.1152/ajpcell.1992.263.2.C365

Laver, D.R. 2006. Regulation of ryanodine receptors from skeletal and cardiac muscle during rest and excitation. *Clin. Exp. Pharmacol. Physiol.* 33:1107–1113. https://doi.org/10.1111/j.1440-1681.2006.04500.x

Lee, J.M., S.H. Rho, D.W. Shin, C. Cho, W.J. Park, S.H. Eom, J. Ma, and D.H. Kim. 2004. Negatively charged amino acids within the intraluminal loop of ryanodine receptor are involved in the interaction with triadin. *J. Biol. Chem.* 279:6994–7000. https://doi.org/10.1074/jbc.M312446200

Lefebvre, R., C. Legrand, E. González-Rodríguez, L. Groom, R.T. Dirksen, and V. Jacquemond. 2011. Defects in Ca²⁺ release associated with local expression of pathological ryanodine receptors in mouse muscle fibres. *J. Physiol.* 589:5361–5382. https://doi.org/10.1113/jphysiol.2011.216408

Legrand, C., E. Giacomello, C. Berthier, B. Allard, V. Sorrentino, and V. Jacquemond. 2008. Spontaneous and voltage-activated Ca²⁺ release in adult mouse skeletal muscle fibres expressing the type 3 ryanodine

Sanchez et al.
Triadic Ca²⁺ changes in skeletal muscle

Journal of General Physiology
https://doi.org/10.1085/jgp.202012592

19 of 20

receptor. *J. Physiol.* 586:441–457. https://doi.org/10.1113/jphysiol.2007.145862

Lyfenko, A.D., S. Ducreux, Y. Wang, L. Xu, F. Zorzato, A. Ferreiro, G. Meissner, S. Treves, and R.T. Dirksen. 2007. Two central core disease (CCD) deletions in the C-terminal region of RYR1 alter muscle excitation-contraction (EC) coupling by distinct mechanisms. *Hum. Mutat.* 28:61–68. https://doi.org/10.1002/humu.20409

Manno, C., L.C. Figueroa, D. Gillespie, R. Fitts, C. Kang, C. Franzini-Armstrong, and E. Rios. 2017. Calsequestrin depolymerizes when calcium is depleted in the sarcoplasmic reticulum of working muscle. *Proc. Natl. Acad. Sci. USA.* 114:E638–E647. https://doi.org/10.1073/pnas.1620265114

Meissner, G. 2002. Regulation of mammalian ryanodine receptors. *Front. Biosci.* 7:d2072–d2080. https://doi.org/10.2741/A899

Murayama, T., and Y. Ogawa. 1992. Purification and characterization of two ryanodine-binding protein isoforms from sarcoplasmic reticulum of bullfrog skeletal muscle. *J. Biochem.* 112:514–522. https://doi.org/10.1093/oxfordjournals.jbchem.a123931

Palade, P., and J. Vergara. 1982. Arsenazo III and antipyrylazo III calcium transients in single skeletal muscle fibers. *J. Gen. Physiol.* 79:679–707. https://doi.org/10.1085/jgp.79.4.679

Pape, P.C., J. De-Shien, and W.K. Chandler. 1995. Calcium release and its voltage dependence in frog cut muscle fibers equilibrated with 20 mM EGTA. *J. Gen. Physiol.* 106:259–336. https://doi.org/10.1085/jgp.106.2.259

Raymackers, J.M., P. Gailly, M.C. Schoor, D. Pette, B. Schwaller, W. Hunziker, M.R. Celio, and J.M. Gillis. 2000. Tetanus relaxation of fast skeletal muscles of the mouse made parvalbumin deficient by gene inactivation. *J. Physiol.* 527:355–364. https://doi.org/10.1111/j.1469-7793.2000.00355.x

Rebbeck, R.T., Y. Karunasekara, P.G. Board, N.A. Beard, M.G. Casarotto, and A.F. Dulhunty. 2014. Skeletal muscle excitation-contraction coupling: who are the dancing partners? *Int. J. Biochem. Cell Biol.* 48:28–38. https://doi.org/10.1016/j.biocel.2013.12.001

Rossi, D., T. Murayama, I. Manini, D. Franci, Y. Ogawa, and V. Sorrentino. 2007. Expression and functional activity of ryanodine receptors (RyRs) during skeletal muscle development. *Cell Calcium.* 41:573–580. https://doi.org/10.1016/j.ceca.2006.10.007

Rossi, D., A.M. Scarcella, E. Liguori, S. Lorenzini, E. Pierantozzi, C. Kutchukian, V. Jacquemond, M. Messa, P. De Camilli, and V. Sorrentino. 2019. Molecular determinants of homo- and heteromeric interactions of Junctophilin-1 at triads in adult skeletal muscle fibers. *Proc. Natl. Acad. Sci. USA.* 116:15716–15724. https://doi.org/10.1073/pnas.1820980116

Sanchez, C., C. Berthier, B. Allard, J. Perrot, C. Bouvard, H. Tsutsui, Y. Okamura, and V. Jacquemond. 2018. Tracking the sarcoplasmic reticulum membrane voltage in muscle with a FRET biosensor. *J. Gen. Physiol.* 150:1163–1177. https://doi.org/10.1085/jgp.201812035

Sárközi, S., P. Szentesi, I. Jona, and L. Csernoch. 1996. Effects of cardiac glycosides on excitation-contraction coupling in frog skeletal muscle fibres. *J. Physiol.* 495:611–626. https://doi.org/10.1113/jphysiol.1996.sp021620

Schuhmeier, R.P., B. Dietze, D. Ursu, F. Lehmann-Horn, and W. Melzer. 2003. Voltage-activated calcium signals in myotubes loaded with high concentrations of EGTA. *Biophys. J.* 84:1065–1078. https://doi.org/10.1016/S0006-3495(03)74923-6

Shang, W., F. Lu, T. Sun, J. Xu, L.L. Li, Y. Wang, G. Wang, L. Chen, X. Wang, M.B. Cannell, et al. 2014. Imaging Ca^{2+} nanosparks in heart with a new targeted biosensor. *Circ. Res.* 114:412–420. https://doi.org/10.1161/CIRCRESAHA.114.302938

Shirokova, N., J. García, and E. Ríos. 1998. Local calcium release in mammalian skeletal muscle. *J. Physiol.* 512:377–384. https://doi.org/10.1111/j.1469-7793.1998.377be.x

Sorrentino, V. 2011. Sarcoplasmic reticulum: structural determinants and protein dynamics. *Int. J. Biochem. Cell Biol.* 43:1075–1078. https://doi.org/10.1016/j.biocel.2011.04.004

Sztretye, M., J. Yi, L. Figueroa, J. Zhou, L. Royer, P. Allen, G. Brum, and E. Ríos. 2011. Measurement of RyR permeability reveals a role of calsequestrin in termination of SR Ca^{2+} release in skeletal muscle. *J. Gen. Physiol.* 138:231–247. https://doi.org/10.1085/jgp.201010592

Tsugorka, A., E. Ríos, and L.A. Blatter. 1995. Imaging elementary events of calcium release in skeletal muscle cells. *Science.* 269:1723–1726. https://doi.org/10.1126/science.7569901

Woods, C.E., D. Novo, M. DiFranco, J. Capote, and J.L. Vergara. 2005. Propagation in the transverse tubular system and voltage dependence of calcium release in normal and mdx mouse muscle fibres. *J. Physiol.* 568:867–880. https://doi.org/10.1113/jphysiol.2005.089318

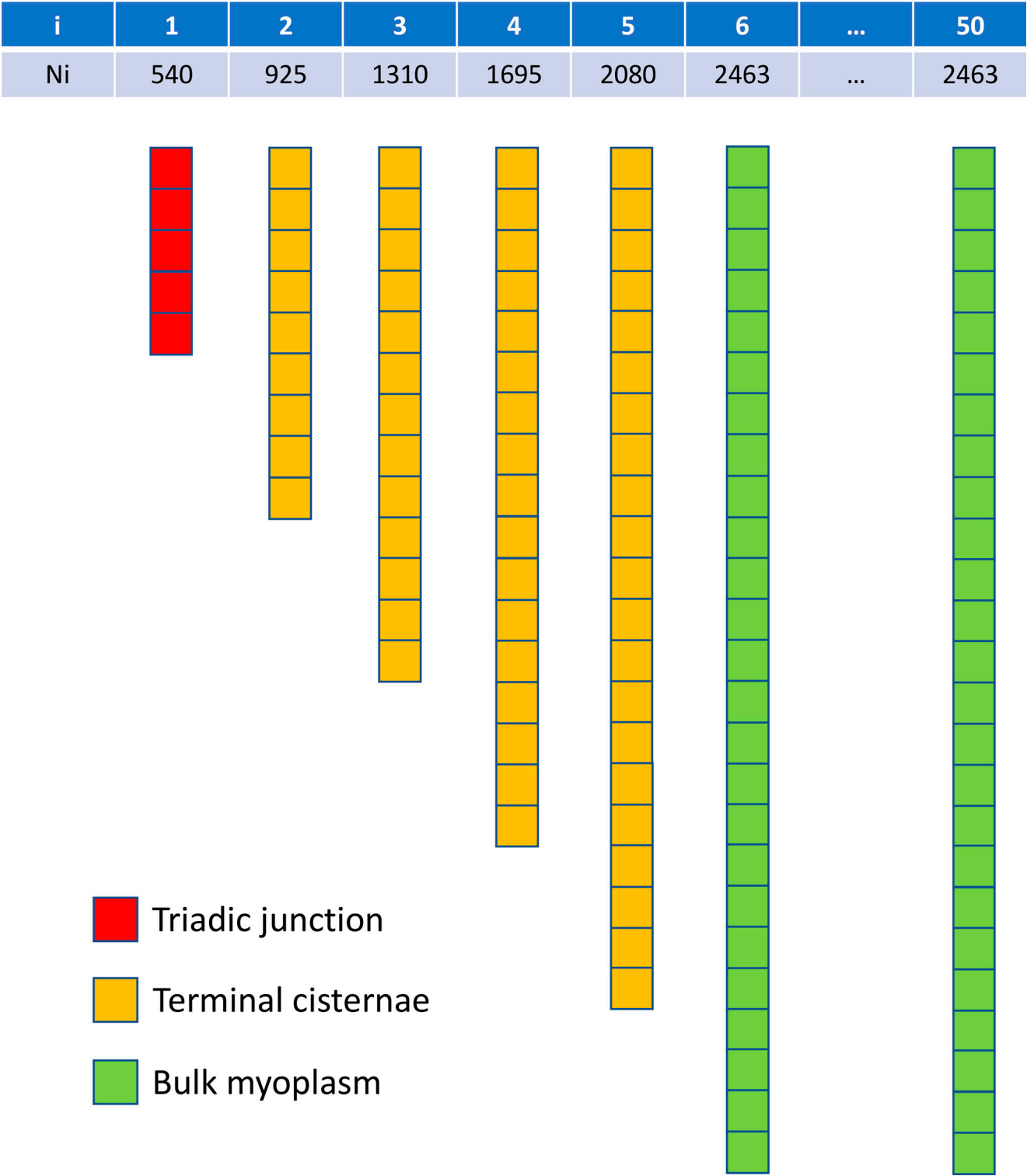| i	1	2	3	4	5	6	...	50
Ni	540	925	1310	1695	2080	2463	...	2463

Figure S1. **Voxel map presenting the distribution of the spatial positions used for simulating the changes in Ca²⁺ and Ca²⁺ bound to GCaMP6f or T306-GCaMP6f along half a sarcomere following a synthetic input Ca²⁺ release flux occurring at the triadic junction.** Ni corresponds to the number of voxels at each position (see Materials and methods).
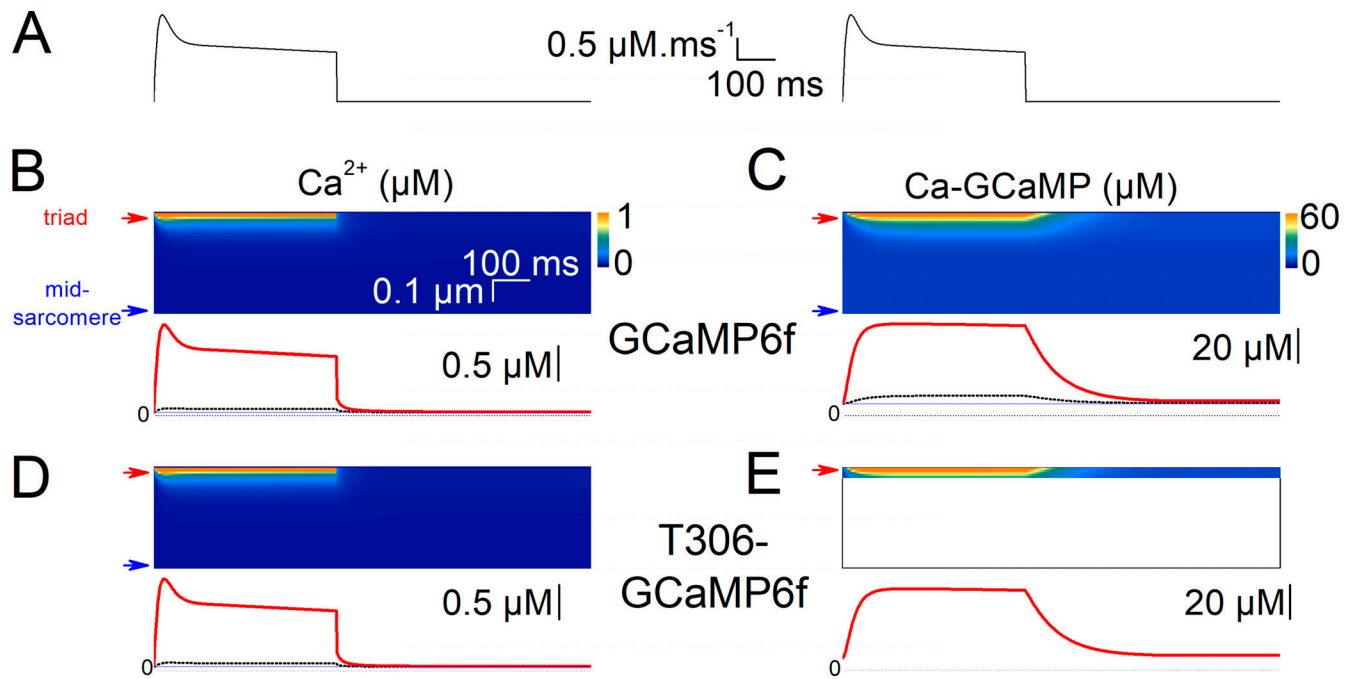
Figure S2. **Model simulation of the spatial gradient of Ca²⁺ and of calcium bound to the GCaMP6f probes along a 0.5-μm distance from the Ca²⁺ release site following a low level of SR Ca²⁺ release activation, assuming a low Ca²⁺ diffusion coefficient. (A)** Synthetic Ca²⁺ release input flux. **(B and C)** Spatial gradient of Ca²⁺ change (B) and corresponding Ca²⁺ bound to GCaMP6f (C). **(D and E)** Spatial gradient of Ca²⁺ change (D) and corresponding Ca²⁺ bound to T306-GCaMP6f (E). In B–E, traces underneath the image show the time course of change in the given parameter at the triad level (thick red trace), at the mid-sarcomere level (thin blue trace), and the average change throughout the distance (dotted black trace).
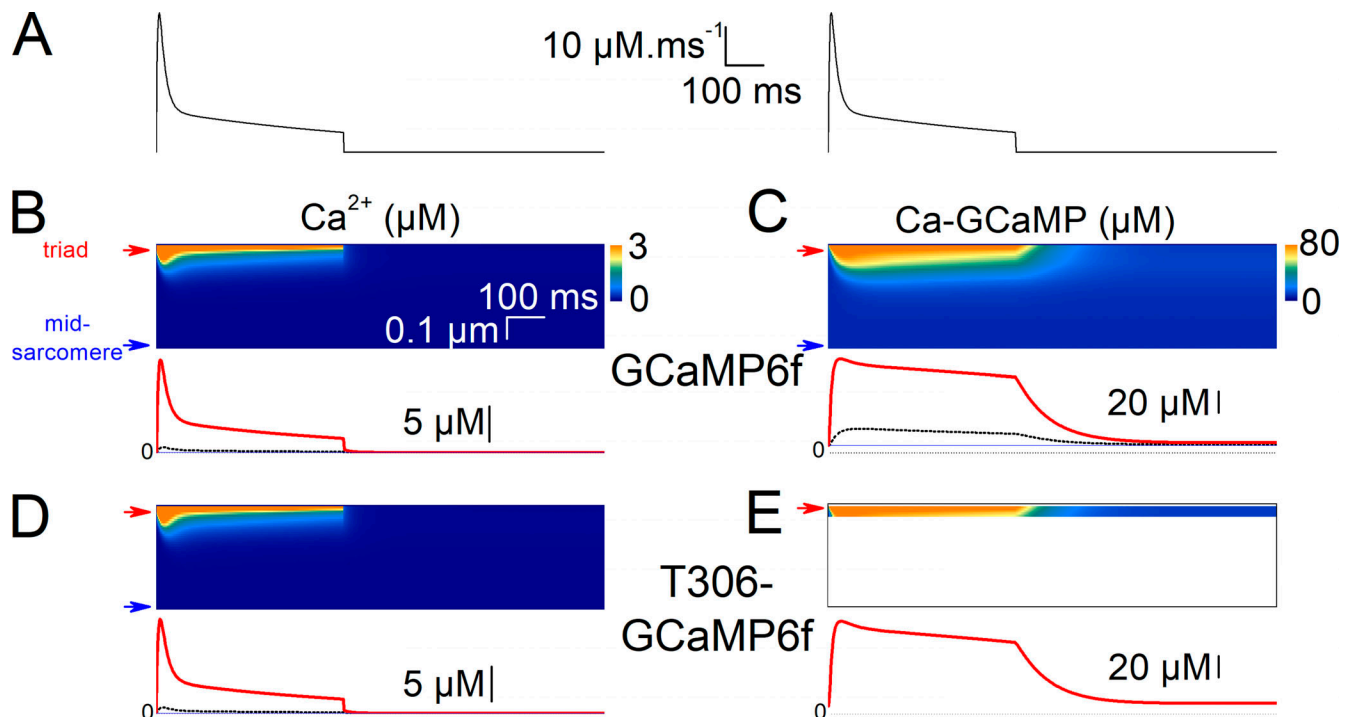
Figure S3. **Model simulation of the spatial gradient of Ca²⁺ and calcium bound to the GCaMP6f probes along a 0.5-μm distance from the Ca²⁺ release site following a large level of SR Ca²⁺ release activation, assuming a low Ca²⁺ diffusion coefficient. (A)** Synthetic Ca²⁺ release input flux. **(B and C)** Spatial gradient of Ca²⁺ change (B) and corresponding Ca²⁺ bound to GCaMP6f (C). **(D and E)** Spatial gradient of Ca²⁺ change (D) and corresponding Ca²⁺ bound to T306-GCaMP6f (E). In B–E, traces underneath the image show the time course of change in the given parameter at the triad level (thick red trace), at the mid-sarcomere level (thin blue trace), and the average change throughout the entire distance (dotted black trace).
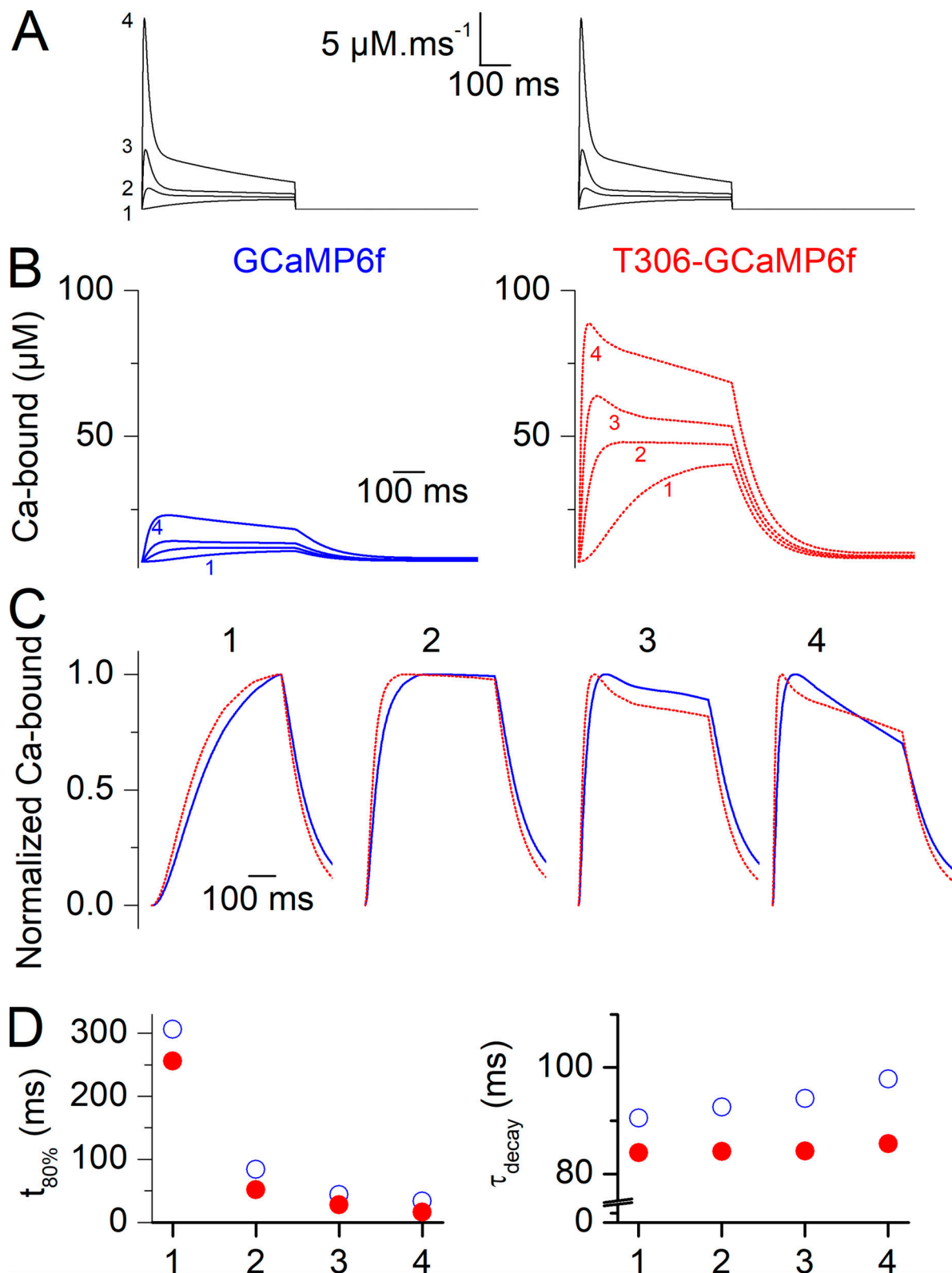
Figure S4. Model simulation of the average changes in Ca²⁺ bound to GCaMP6f and T306-GCaMP6f following different levels of SR Ca²⁺ release activation, assuming a low Ca²⁺ diffusion coefficient. (A) Superimposed synthetic Ca²⁺ release input fluxes used for the simulation (1–4). **(B)** Calculated average changes in Ca²⁺ bound to GCaMP6f (left, blue) or T306-GCaMP6f (right, red) following each of the four Ca²⁺ release input fluxes shown in A. **(C)** Normalized time course of the calculated average changes in Ca²⁺ bound to GCaMP6f (continuous blue traces) and T306-GCaMP6f (dotted red traces) in response to the Ca²⁺ release fluxes shown in A. Changes in Ca²⁺ bound to each of the two probes for a same given input flux are shown superimposed. **(D)** Dependence upon the input flux (1–4) of the time to reach 80% of the peak change in Ca²⁺ bound to GCaMP6f (left, open blue circles) and T306-GCaMP6f (filled red circles) and corresponding values for the time constant of decay (right) after the end of the release flux.
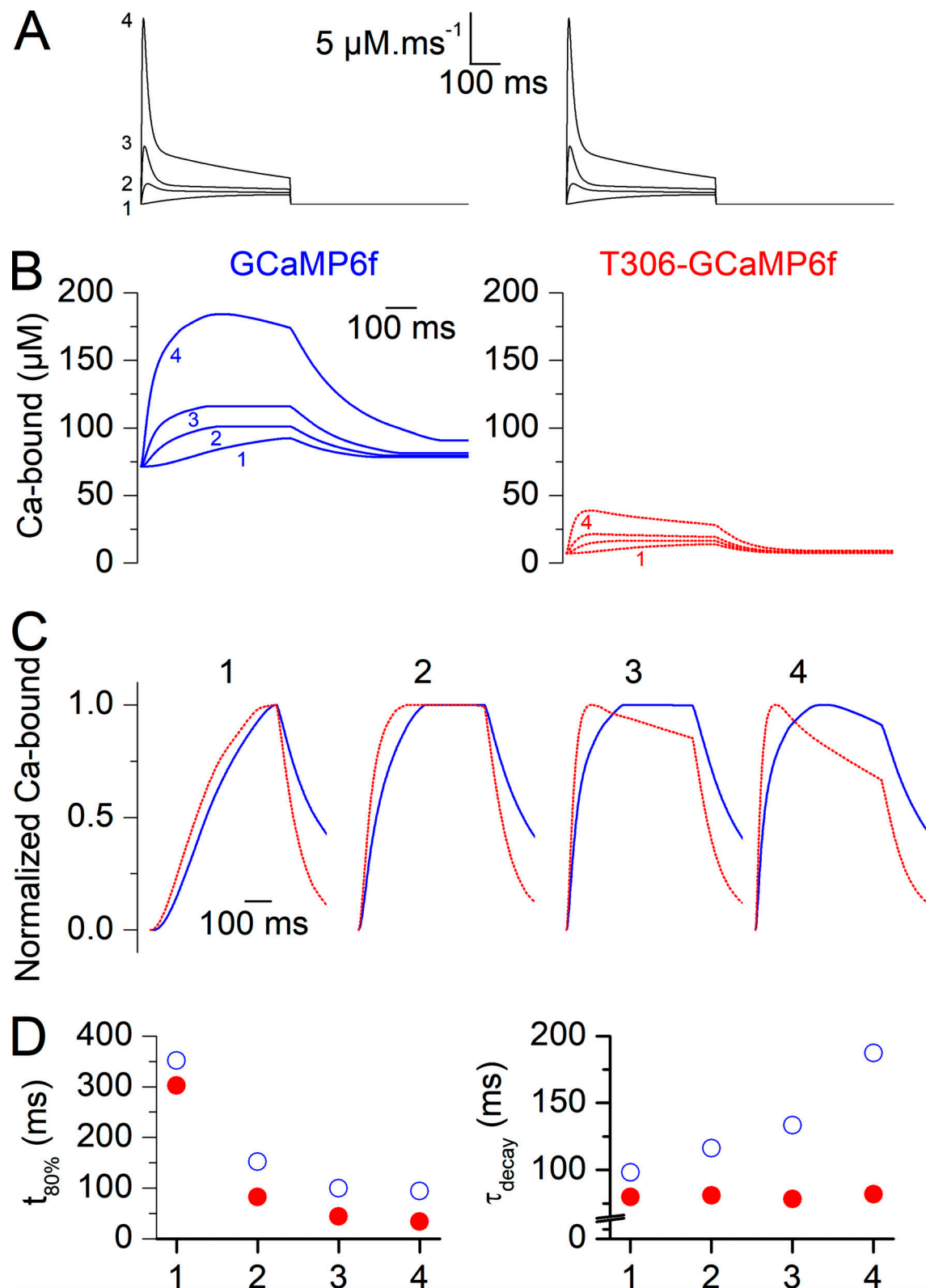
Figure S5. **Model simulation of the average changes in Ca²⁺ bound to GCaMP6f and T306-GCaMP6f, assuming the concentration of GCaMP6f to be 10 times larger than that of T306-GCaMP6f. (A)** Superimposed synthetic Ca²⁺ release input fluxes used for the simulation (1–4). **(B)** Calculated average changes in Ca²⁺ bound to GCaMP6f (left, blue) or T306-GCaMP6f (right, red) following each of the four Ca²⁺ release input fluxes shown in A. **(C)** Normalized time course of the calculated average changes in Ca²⁺ bound to GCaMP6f (continuous blue traces) and T306-GCaMP6f (dotted red traces) in response to the Ca²⁺ release fluxes shown in A. Changes in Ca²⁺ bound to each of the two probes for a same given input flux are shown superimposed. **(D)** Dependence upon the input flux (1–4) of the time to reach 80% of the peak change in Ca²⁺ bound to GCaMP6f (left, open blue circles) and T306-GCaMP6f (filled red circles) and corresponding values for the time constant of decay (right) after the end of the release flux.